

8-2014

Can Tidal Perturbations Associated with Sea Level Variations in the Western Pacific Ocean be used to Understand Future Effects of Tidal Evolution?

Adam T. Devlin
Portland State University


David A. Jay
Portland State University, djay@pdx.edu

Stefan A. Talke
Portland State University, talke@pdx.edu

Edward D. Zaron
Portland State University, ezaron@pdx.edu

Let us know how access to this document benefits you.

Follow this and additional works at: https://pdxscholar.library.pdx.edu/cengin_fac

 Part of the [Civil Engineering Commons](#), and the [Environmental Engineering Commons](#)

Citation Details

Devlin, Adam T.; Jay, David A.; Talke, Stefan A.; and Zaron, Edward D., "Can Tidal Perturbations Associated with Sea Level Variations in the Western Pacific Ocean be used to Understand Future Effects of Tidal Evolution?" (2014). *Civil and Environmental Engineering Faculty Publications and Presentations*. 173.

https://pdxscholar.library.pdx.edu/cengin_fac/173

This Post-Print is brought to you for free and open access. It has been accepted for inclusion in Civil and Environmental Engineering Faculty Publications and Presentations by an authorized administrator of PDXScholar. For more information, please contact pdxscholar@pdx.edu.

1 Can tidal perturbations associated with sea level
2 variations in the western Pacific Ocean be used to
3 understand future effects of tidal evolution?
4
5

6 Adam T. Devlin^a,

7 David A. Jay^a, Stefan A. Talke^a, Edward Zaron^a

8
9 ^a(Portland State University, Civil & Environmental Engineering
10 PO Box 751 Portland, OR 97207-0751)

11 *Corresponding author Tel.: (734) 776-1284

12 E-mail addresses: devlina@pdx.edu (A.T. Devlin), djay@cecs.pdx.edu (D.A. Jay),
13 stefant@cecs.pdx.edu (S.A. Talke), zaron@cecs.pdx.edu (E. Zaron)

14
15 April 2014

16 Submitted to:

17 Ocean Dynamics

18 **Keywords:**

19 Astronomical tides; Western tropical Pacific; sea level variability; tidal anomaly trends; climate
20 change; resonant triads

22 Abstract

23 This study examines connections between mean sea level (MSL) variability and diurnal and semidiurnal tidal
24 constituent variations at 17 open-ocean and 9 continental shelf tide gauges in the western tropical Pacific Ocean, a
25 region showing anomalous rise in MSL over the last 20 years and strong interannual variability. Detrended MSL
26 fluctuations are correlated with detrended tidal amplitude and phase fluctuations, defined as tidal anomaly trends
27 (TATs), to quantify the response of tidal properties to MSL variation. About 20 significant amplitude and phase TATs
28 are found for each of the two strongest tidal constituents, K_1 (diurnal) and M_2 (semidiurnal). Lesser constituents (O_1
29 and S_2) show trends at nearly half of all gauges. Fluctuations in MSL shift amplitudes and phases; both positive and
30 negative responses occur. Changing overtimes suggest TATs are influenced by changing shallow water friction over
31 the equatorial Western Pacific and the eastern coast of Australia (especially near the Great Barrier Reef). There is a
32 strong connection between semidiurnal TATs at stations around the Solomon Islands and changes in thermocline
33 depth, overtide generation, and the El Niño Southern Oscillation (ENSO). TATs for O_1 , K_1 and M_2 are related to each
34 other in a manner that suggests transfer of energy from M_2 to the two diurnals via resonant triad interactions; these
35 cause major tidal variability on sub-decadal time scales, especially for M_2 . The response of tides to MSL variability
36 is not only spatially complex, it is frequency dependent; therefore, short-term responses may not predict long-term
37 behavior.

38

39 1. Introduction

40 This study examines the connections between mean sea level (MSL) rise and variations in major diurnal and
41 semidiurnal tidal constituent properties at open-ocean and continental shelf tide gauges in the Western Tropical Pacific
42 Ocean, a region showing anomalous MSL rise over the last 20 years (Merrifield, 2011). Additionally, this domain
43 exhibits large excursions of interannual sea level and tidal variability, especially during El Niño and La Niña events.
44 We attempt to answer the question posed in the title, can we use the relations of the observed short-term MSL
45 fluctuations to the short-term tidal variations to understand the future effects of tidal evolution, and to predict changes
46 in total water level (MSL + tides) under higher MSL conditions? MSL rise rates have increased since ca. 1993 at 15
47 of 26 gauges used in this study, and the rate has increased at both deep ocean island stations and at continental shelf
48 gauges (Figure 1; Tables 1a and 1b). This rapid increase in Western Pacific MSL rate of change provides an
49 opportunity to seek connections between MSL rise and tidal evolution. If MSL rise is a primary driver of changes in
50 the tides, as suggested by Arbic and Garrett (2010), then this area should exhibit unusually large rates of tidal evolution
51 over the same time period, with a relatively simple spatial pattern. Alternatively, if changes in internal wave
52 propagation (as in Hawaii, Colosi and Munk, 2006) are dominant, then smaller-scale, less spatially coherent tidal
53 evolution would be expected. Shallow water frictional processes can also alter tidal constituents and may be altered
54 by MSL variations (Amin, 1983), but this local process would not likely drive regional trends. Finally, the existence
55 of multiple mechanisms could lead to complex patterns of tidal evolution, and this is, in fact, what our examination of

56 Pacific Island gauges suggests. Furthermore, the results of our analyses suggest that different processes are active in
57 different parts of the frequency spectrum, and so the behavior of short-term fluctuations do not, in general, allow a
58 clear prediction of what may be expected for long-term trends of tidal properties.

59 We examine the interactions of detrended tidal anomalies—the deviations from long-term trends in tidal
60 constituent properties—in relation to detrended MSL anomalies (deviations from long-term MSL trends) as a means
61 of diagnosing dynamical factors that might influence the longer-term evolution of tides. Specifically, we examine
62 MSL anomalies and tidal anomalies at 26 tide gauges in the Western Pacific region, at both island gauges, and at
63 nearby continental shelves. We focus on four constituents, the two largest semidiurnal (twice daily) constituents, M_2
64 (twice daily lunar tide) and S_2 (twice daily solar tide), and the two largest diurnal (once daily) components, K_1
65 (lunisolar diurnal) and O_1 (lunar diurnal). In addition, a subset of gauges with a minimum length-of-record (LOR)
66 ≥ 40 yr is used to determine whether any changes in tidal trends are associated with the onset of anomalous regional
67 MSL rise in recent decades. We will compare the long-term linear trends of both MSL and tidal properties (amplitude
68 and phase), as well as the shorter-term fluctuations of MSL anomalies and tidal property anomalies from these long
69 term trends (LTTs). Under rapidly rising and warming sea level scenarios, tidal amphidromes may shift as MSL rises
70 and stratification increases (Pugh, 2004, Müller 2010). Amphidromes may shift center position, amplify, and/or rotate.
71 For all four tides, we will compare the changes in amplitudes and phases with changes in MSL in the context of
72 possible amphidromic migrations.

73 We will also attempt to identify the mechanisms behind the observed trends in tidal properties in several
74 ways. First, we consider non-linear, shallow-water overtides as a tool for understanding changing friction over
75 continental shelves and in shallow water regions in relation to changing tides. Then we will compare the variations of
76 tidal trends at select stations to fluctuations in regional thermocline depth. Finally, we will consider the possibility of
77 a resonant triad interaction between the K , O_1 , and M_2 tides.

78 **2. Background**

79 **2.1. Changing sea level and changing tides**

80 Ocean tides are usually considered stationary in time because of their close relationship to astronomical
81 forcing. However, recent work has shown that tides are evolving at diverse rates in different parts of the ocean without
82 any apparent relationship to astronomical forcing (Woodworth, 2010). Changes in major tidal constituents such as M_2 ,
83 S_2 , K_1 and O_1 are observed in the Eastern Pacific (Jay, 2009), the Gulf of Maine (Ray, 2006), and the North Atlantic
84 (Ray, 2009; Müller et al., 2011). Changes in tidal range and datum levels along many parts of the US coast line (Flick
85 et al., 2003) also indicate evolution of constituents. While several mechanisms have been suggested that are
86 independent of mean sea level (MSL) rise (Jay 2009), MSL may influence or be correlated with tidal evolution in a
87 variety of ways, both locally and on amphidromic scales, as well as over a multitude of frequency bands, from seasonal
88 to multi-decadal. One possibility is that changes in continental shelf depth may influence tides on a basin scale (Arbic
89 and Garrett, 2010, Arbic et al., 2009), through changing bed friction in shallow water. Rising MSL also alters tidal

90 wavelength and wave speed in shallow water areas, and reduces energy dissipation due to the reduced effect of bottom
91 friction (Pugh, 1987). Alternatively, MSL rise may coincide with changes in stratification and/or thermocline depth.
92 These internal changes may alter the surface manifestation of internal tides in ways that are detectable at tide gauges,
93 e.g., at Honolulu (Colosi and Munk, 2006). Finally, fluctuations in multiple constituents may be related via resonant
94 triads (cf. Lamb, 2007). These factors, individually or in combination, could lead to a migration of the tidal
95 amphidromes that would appear as a change in tidal properties at fixed observation stations.

96 The long-term global average trend in MSL is 1.7 ± 0.3 mmyr⁻¹, as determined from tide gauge records
97 (Church and White, 2006; 2011). Satellite observations show that the global MSL rise since 1993 has been 3.3 ± 0.4
98 mmyr⁻¹ (Nicholls and Cavenaze, 2010), suggesting a recent acceleration. However, MSL rise is spatially non-uniform.
99 Five-year running means suggest that the MSL trend in the western Tropical Pacific has approached +10 mmyr⁻¹ at
100 some locations since 1993 (Merrifield, 2011). In contrast, MSL rise rates in the Northeastern Pacific have been below
101 the global average over the same time period (National Research Council Ocean Science Board, 2012), with some
102 places along the West Coast of the US having constant or slightly negative rates since 1980, partly due to prevailing
103 wind patterns. While it is unlikely that the extreme rise rate in the western tropical Pacific will persist, and Bromirski
104 et al. (2011) have suggested that a trend reversal along the US West Coast is imminent, such decadal-scale variations
105 in MSL rise rates offer an opportunity to examine the connections between different parts of the water level spectrum,
106 in this case, between tidal evolution and MSL.

107 MSL also exhibits fluctuations related to climate cycles. The El-Nino Southern Oscillation (ENSO) is a
108 strong contributing factor to sea surface anomalies in the Pacific (Kohl et al. 2007; Lombard et al. 2009; Timmermann
109 et al. 2010), and local, short-term MSL anomalies associated with ENSO are often much larger than long-term trends.
110 The 1982-1983 and the 1997-1998 El Nino events gave rise to widespread MSL fluctuations, with some coastal
111 localities showing yearly averaged MSL rises or falls of 200mm or more (Nerem et al, 1999; White et al, 2001).
112 ENSO-related sea surface height (SSH) trends are, however, an order of magnitude too small (over a ~15yr time
113 period) and too transient to account for the observed MSL rise for the western tropical Pacific region (Merrifield,
114 2011). Instead, Merrifield argues that the unusually rapid MSL rise in the western tropical Pacific is correlated with
115 changing wind stress patterns in the region from after 1993, corresponding roughly to the period of satellite
116 observations. ENSO related sea level variability is difficult to remove entirely from MSL time series, due to its quasi-
117 periodic behavior, and large geographical extent that the signal affects. Hamlington, et al. (2011) present a detailed
118 study on the capture and removal of the ENSO signal and of modulated annual variability from global sea level records
119 for 1950 through 2009, using cyclostationary empirical orthogonal function techniques, based on the methods of
120 Church et al. (2004).

121 Predictions of future inundation due to extreme events must account for both MSL rise and changes in tidal
122 properties. For example, Haigh et al. (2010) found that MSL rise rates of +0.8-2.3 mmyr⁻¹ in the English Channel
123 were accompanied by smaller increases in high water elevation of +0.1-0.3 mmyr⁻¹ (relative to MSL). A numerical
124 model from Pickering et al. (2012) found that a 2m increase in MSL increased the spring tidal range from -0.49m to

125 +0.35m, depending on location. Hence, changing tidal processes can either mitigate or exacerbate changes to extreme
 126 water levels caused by MSL rise (Horsburgh and Wilson, 2007).

127 Changing internal tides are a likely mechanism connecting MSL change and the tidal evolution, at least
 128 between the critical latitudes for the major tidal species, $\pm 30^\circ$ latitude for K_1 and, and $\pm 75^\circ$ for M_2 . Ray and Mitchum
 129 (1997) report that time-series of the monthly variations of M_2 and MSL were coherent at annual, inter-annual and
 130 intra-annual bands, and Mitchum and Chiswell (2000) note that higher amplitudes of M_2 are associated with times of
 131 a deeper thermocline. Colosi and Munk (2006) conclude that the observed increase in the total M_2 amplitude from
 132 161mm to 169mm at Honolulu over the past century occurred because the internal M_2 wave moved more closely into
 133 phase with the surface tide. This conclusion is dependent on the assumption that rising sea level is a proxy for a deeper
 134 thermocline, which then alters the phase and/or the amplitudes of the internal tide.

135 2.2 Resonant Triads-- Theory

136 Resonant triad interactions are a possible mechanism for coherent fluctuations of multiple tidal constituents.
 137 Resonant (and near-resonant) triad interactions, were first described in the context of light waves by Armstrong et al
 138 (1962), discussed generally by Bretherton (1964), and solutions for water waves are detailed by Craik (1985).
 139 Resonant internal wave triads arise from the (nonlinear) convective acceleration terms and are essential to energy
 140 transfer across the oceanic tidal spectrum (Hibiya et al 2002; Gerkama et al, 2006), including shoaling surface gravity
 141 waves in shallow water (Frelich and Guza, 1984), and are involved in parametric subharmonic instabilities (PSI) at or
 142 near critical latitudes (McKinnon and Winters, 2005).

143 A resonant triad is a pathway for an energy conserving, nonlinear energy exchange between multiple wave
 144 modes. The three (or more) complex plane waves involved in a triad have the form:

$$145 \quad Z_j(t) = A_j(t) \exp[i\theta_j(t)] \quad (1)$$

$$\text{with : } \theta_j = (\mathbf{k}_j \cdot \mathbf{x} - \omega_j t) = (k_j x + l_j y + m_j z - \omega_j t)$$

146 The ω_j 's are the frequencies of each wave; $\mathbf{k}_j = (k_j, l_j, m_j)$ are the wavevectors of each wave, and each wave has a
 147 dispersion relation given by $\omega_j(\mathbf{k}_j)$. For three interacting waves, the main resonance conditions are (Craik, 1985;
 148 Simmons, 1969) that the waves are phase locked (i.e., the sum of the phases is a constant), and that the frequencies
 149 and wavenumbers are also matched via a summation. Thus:

$$150 \quad \theta_1 + \theta_2 + \theta_3 = C, \quad (2a)$$

$$151 \quad \omega_1 \pm \omega_2 \pm \omega_3 = \Delta\omega,$$

$$\mathbf{k}_1 \pm \mathbf{k}_2 \pm \mathbf{k}_3 = \Delta\mathbf{k} \quad [\text{for : } \mathbf{k} = (k, l, m)] \quad (2b, c)$$

152 Small frequency and wavenumber mismatches ($\Delta\omega$ and $\Delta\mathbf{k}$) allow for the possibility of near-resonant triads
 153 (Craik, 1985); exact triads have $\Delta\omega=0$ and $\Delta\mathbf{k}=0$. Near-resonant triads are possible in the ocean for internal tide
 154 generation at or near topographic features (Lamb, 2007). These relationships hold for a single triad of three waves,
 155 but are applicable to multiple triads of three waves, or even groups of four waves (tetrads). While Eq. (2b) is satisfied
 156 exactly ($\Delta\omega=0$) by a number of tidal constituent combinations, Eq. (2c) is geometry-dependent. The dispersion
 157 relationship, $\omega_i(\mathbf{k}_i)$, for planar and linear internal waves in the ocean is given by (Gill, 1982):

$$158 \quad \omega_j(\mathbf{k}_j)^2 = \frac{N^2(k_j^2 + l_j^2) + f^2 m_j^2}{k_j^2 + l_j^2 + m_j^2} \quad (3)$$

159 Where N indicates the buoyancy frequency, and f is the Coriolis frequency; f is a constant for each gauge, while N is
 160 dependent on the local depth profile of temperature and salinity, and may vary seasonally.

161 There are more than 450 tidal frequencies in the ocean (Cartwright and Tayler, 1971); many of these
 162 frequencies could in theory form triads that satisfy Eq. (2b), but most such triads are based on minor tidal constituents
 163 and are unlikely to be energetic enough to be measurable. The triad most likely to be detected consists of K_1 , O_1 and
 164 M_2 . The K_1 and O_1 tidal frequencies are close to each other, being equidistant (plus or minus ~2%) from half the M_2
 165 frequency; in terms of M_2 , they are:

$$166 \quad \omega_{m_2} = \omega_{k_1} + \omega_{o_1} \quad (4)$$

$$(\omega_{k_1} = 0.52\omega_{m_2}); (\omega_{o_1} = 0.48\omega_{m_2})$$

167 We note that shallow water (frictional) overtides satisfy Eqs. (2a) and (2b), and may satisfy Eq. (2c).

168 Ball (1964) details how triad interactions can occur at the interface of a two-layer fluid, e.g., at the
 169 thermocline. The strength of the interactions is dependent on the depths of the layers as well as the stratification and
 170 the angles of incidence of each wave relative to the thermocline interface. Recent upper-layer warming in the Western
 171 Pacific (Domingues et al, 2008) may be leading to a deepening thermocline and stronger stratification (Müller, 2012),
 172 which makes the ocean effectively two-layered, and enhanced triad interactions may occur at the interface. MSL rise
 173 may also cause an extension in a basin's areal extent, as new areas are inundated. The close frequencies of K_1 and O_1
 174 will yield similar wavenumber vectors for any given mode. In addition, because they are both nearly half the M_2
 175 frequency, internal modes of K_1 and O_1 may energy exchange via M_2 . Alternatively, remote changes in barotropic
 176 M_2 may alter low-mode diurnal internal tides via parametric subharmonic instability (MacKinnon and Winters, 2005).
 177 Both possibilities are explored below.

178 **3. Methods**

179 **3.1. Station Selection and Data**

180 Twenty-two of the 26 tidal records used in this study were selected from the University of Hawaii Sea Level
181 Center (UHSLC) archives. The Australian stations of Cairns, Gladstone, and Williamstown were provided by the
182 Australian National Tidal Center and Auckland, New Zealand was provided by Land Information New Zealand
183 (LINZ). The factors that guided our station selection were:

- 184 1) Location: all stations are in or near the area of anomalous MSL rise.
- 185 2) Temporal coverage: all stations used have an LOR (length of record) greater than one nodal cycle
186 (18.6yrs); LOR ranged from 19 to 107yrs.
- 187 3) Completeness: the data were more than 80% complete over the record.

188 There were 17 island and 9 coastal stations that met these criteria, allowing comparison of open-ocean and continental
189 shelf dynamics. Locations are shown in Figure 1, along with bathymetry. Figure 2 shows yearly average MSL time
190 series at 7 long-term gauges (Guam, Pago Pago, Kwaljein, Malakal, Yap, Honiara, Kanton). These suggest a break in
191 sea level trend at or around 1993 (broken vertical line). All of these 7 gauges and more than half of the 26 total gauges
192 of our study show an increase in MSL rate after this point up to the present. The longer-period gauges used will be
193 subject to larger timing errors in the earlier years of the records, but these clock errors have improved in the recent
194 decades with the advent of precise GPS clocks. A detailed discussion of the effect of clock errors in the Western
195 Pacific can be found in: (Zaron and Jay, 2014).

196 Table 1a shows the gauges used (location name and country), start and end year of the complete length of
197 record (LOR), and a descriptor indicating the environment where the gauge is located. For islands, delineation is made
198 between low-lying atolls, steep islands with active volcanism, and non-volcanic mountainous terrain. Locations where
199 a coral reef surrounds one or both sides of the island are also indicated. For coastal locations, we note whether the
200 gauge location involves a river estuary, or a coastal enclosed bay. The last three columns of Table 1a show the MSL
201 rates, expressed in mmyr^{-1} , shown first for the entire record, and then for the years before 1993, and after 1993. Rates
202 are only reported for the early years if there exists at least a full nodal period of data (~19 years), otherwise, they are
203 not calculated, since these determinations may be inaccurate.

204

205 **3.2. Harmonic Analysis and Tidal Admittance**

206 To account for nodal cycle variability, we investigate tidal trends through the use of a tidal admittance.
207 Admittance is a unitless, complex ratio of an observed tidal constituent (m) to its corresponding astronomical
208 equilibrium amplitude, V/g (m); tidal potential V is in m^2s^{-2} and g is the acceleration due to gravity, in ms^{-2} . Because
209 nodal and other low-frequency astronomical variability is present with similar (relative) strength in both the observed
210 tidal record and in V/g , it is largely absent in admittance time series.

211 For all relevant stations, overlapping yearly tidal harmonic analyses (at monthly time steps) were carried out
 212 on hourly records and hourly V/g, using the tidal harmonic analysis package in MATLAB developed by Pawlowicz
 213 (2002), and modified to include robust fitting by Leffler and Jay (2009). The tidal potential is determined using a
 214 program provided by Richard Ray (National Atmospheric and Space Administration, personal communication) that
 215 is based on the methods of Cartwright and Tayler (1971), and Cartwright and Edden (1973). Results from a single
 216 harmonic analysis determine an amplitude, A , and phase, θ , at the central time of the analysis window for each tidal
 217 constituent with error estimates for both. Use of a moving analysis window produces time-series of amplitude and
 218 phase; both monthly (767hr) and annual analyses were used. From amplitude $A(t)$ and phase $\theta(t)$ time series one can
 219 construct complex amplitudes $\mathbf{Z}(t)$,

$$220 \quad \mathbf{Z}(t) = A(t)e^{-i\theta(t)}. \quad (5)$$

221 We form time-series of tidal admittance ratio (AR) and phase difference (PD) for any constituent using Eqs. (6) and
 222 (7),

$$223 \quad \mathbf{AR}(t) = \frac{A_{obs}(t)}{A_{pot}(t)} \quad (6)$$

$$224 \quad \mathbf{PD}(t) = \theta_{obs}(t) - \theta_{pot}(t) \quad (7)$$

225 Where the subscripts ‘obs’ or ‘pot’ denote the the observed data or the equilibrium amplitude, respectively. Both
 226 the admittance ratio in Eq. (6) and the phase difference in Eq. (7) largely remove the nodal-cycle variability,
 227 allowing easier examination of the non-tidal signals.

228 **3.3. Mean Sea Level and Anomaly Trends**

229 The 26 gauges used have a variable time coverage; some have less than 40 years of data, others have 100
 230 years or more. While the long-term trends are an important concern that must still be considered in the overall picture
 231 of the ocean, our primary focus here is the interannual variations of MSL and the tides. MSL time-series are generated
 232 by taking overlapping yearly averages of the original hourly water level data at monthly intervals, without corrections
 233 for local ground motion or inverted barometer effects. AR and PD time series are generated by overlapping yearly
 234 harmonic analyses. We remove trends from the yearly AR, PD, and MSL time-series for each location and constituent
 235 over the entire record. The removed residual trends are fit by linear regression, reported in Table 1a (MSL) and 1b
 236 (ARs and PDs).

237 The removal of the long-term trends leaves us with time-series of residual variations in AR, PD, and MSL,
 238 which are compared with one another (and with other ancillary time-series like thermocline depth), using scatter plots,
 239 cross-correlations, and regression to determine a tidal anomaly trend (TAT) and related statistics (Huber, 1981). The
 240 mean value of the tidal potential at each location is used as a scale factor to convert the non-dimensional TAT into a

241 dimensional amplitude trend (A-TAT, expressed as millimeter change per meter sea level rise (mmm⁻¹). The same
 242 approach is used with the phase difference time-series to provide phase anomaly trends relative to the potential (P-
 243 TAT), with the trends expressed as degree change per meter sea level rise (degm⁻¹).

244 Sample results (Figure 3) show the A-TATs (top 4 panes, (a) - (d)) and P-TATs (bottom 4 panes, (e) – (h))
 245 for the diurnal (K₁ and O₁) and semidiurnal (M₂ and S₂) tides vs. MSL at Honiara, Solomon Islands (9.4167 S, 159.950
 246 E). The scatter plots at Honiara exhibit some of the most coherent trends in our data set, for M₂, with r² > 0.9. While
 247 the M₂ tide amplitude is relatively small at this location (~50mm), the anomaly trend is large, +65.6 ± 3.3 m mm⁻¹
 248 (132% of the local M₂ amplitude per meter of MSL rise). The S₂ trend in amplitude is not as coherent, but is still
 249 significant, as are the K₁ and O₁ A-TATs (Table 2; plots in supplementary materials). Trends in M₂ and S₂ phase are
 250 smaller but still significant (Table 3). The diurnal P-TATs are not significant. A-TAT and P-TAT plots for
 251 semidiurnal and diurnal tides at all 26 stations are provided in supplementary materials (Figures S1-1, through S1-26;
 252 Online Resource 1).

253 **3.4. Friction and Overtides**

254 Overtide generation is superficially similar to a resonant triad interaction, since both may satisfy a similar
 255 frequency condition to Eq. (2b), (i.e., ω₁ + ω₂ = ω₃). Overtides can be linked to bottom topography, but may also
 256 results from internal waves of large amplitude (Legg and Klymak, 2008), or from strong flow curvature (Parker, 1991).
 257 The largest overtide at most locations is M₄, twice the frequency of M₂; M₄ (ω₃) results from the non-linear interaction
 258 of M₂ tidal currents with itself (ω₁ + ω₂). However, the wavenumber condition Eq. (2c) will only be satisfied in certain
 259 cases (Kukulka and Jay, 2003), and is not a requirement. In addition, the driving non-linearity (quadratic bed friction)
 260 is not the same as that for resonant triads (convective accelerations). Still, a frictional triad may interact with a resonant
 261 triad, as can a mean flow or an eddy field (Lelong and Kunze, 2013). It is, therefore, reasonable to suppose constituent
 262 interactions to be part frictional and part resonant. If overtides change substantially over time, it may indicate changes
 263 in non-linear frictional interaction (Parker, 1991). Because M₄ is not represented in the astronomical potential, it is
 264 normalized by an appropriate overtide ratio (OR) to its forcing constituent, M₂,

$$265 \quad OR_{m4}(t) = \frac{A_{m4}(t)}{[A_{m2}(t)]^2} \quad . \quad (8)$$

266 Here, OR_{m4} indicates the overtide ratio of M₄. This ratio is analogous to an admittance calculation and will remove
 267 known long-period variations such as the nodal cycle. Additional overtides investigated are: S₄ (interaction of S₂ with
 268 itself), MK₃ (interaction of M₂ and K₁), M₆ (third harmonic of M₂), MS₄ (interaction of M₂ and S₂), and MO₃
 269 (interaction of O₁ and M₂). In each case, the overtide “ratio” is that between the overtide amplitude and the product
 270 of the amplitudes of the forcing waves. Overtides are small and may not be resolvable against background noise; we
 271 consider only overtides with a signal-to-noise ratio greater than 2.0. Temporal trends are normalized as the percentage
 272 change (per year) from local means of the overtide ratios (ORs). Additionally, we compare time-series of M₄ and M₆

273 overtide ratios at Honiara and Rabaul, two stations where the local overtides are anomalously large, to local MSL
 274 variations, and to the El Nino Southern Oscillation (ENSO) through the use of the Multivariate El Nino Index (MEI),
 275 as defined by the National Oceanic and Atmospheric Administration (NOAA) climate data center:
 276 <http://www.ncdc.noaa.gov>. Note that the Rabaul station was decommissioned in 1997.

277 **3.5 Thermocline Depth and EEMD Analysis**

278 Observed tidal properties are compared to estimated thermocline depths to diagnose the possible role of
 279 internal processes in tidal anomaly trends. Thermocline depths have been synthesized from the NOAA Tropical
 280 Atmosphere Ocean project (TAO) buoys: (<http://www.pmel.noaa.gov/tao/>). The TAO array, established in the early
 281 1990s, is a gridded network of 70 buoys extending from 8°N to 8°S and from 137° E to 95° W. These buoys record
 282 sea surface temperature (SST), wind speed, and air pressure plus water temperature at increments of 25m down to
 283 250m, and also at 300m and 500m. From this profile, the depth of the 20°C isotherm, D_{20} , is estimated and used as a
 284 proxy for thermocline depth. D_{20} time-series are compared to tidal property (AR and PD) time-series for gauges at
 285 Honiara, Pago Pago, and Kapingamarangi, where some of the largest TATs (relative to local mean tides) are seen for
 286 the semidiurnal tides (M_2 and S_2). Monthly averaged D_{20} data are compared to monthly M_2 and S_2 admittance data,
 287 calculated using 767 hour analysis windows in *R_T_Tide*, allowing examination of seasonal, as well as interannual,
 288 variations.

289 The D_{20} and monthly A-TAT time-series are separated into quasi-orthogonal scales using an EEMD
 290 (Ensemble Empirical Mode Decomposition) analysis (Huang, et al., 1998; Huang and Wu, 2008). EEMD uses a
 291 sifting process to split signals into approximately dyadic modes—a signal of length 2^n yields $\sim n$ modes. We selectively
 292 recombine modes to preserve the desired scales of variation (from about annual to decadal scale), while removing
 293 higher frequency variability and the long-term trend. In the language of EEMD, the decomposition of the variables
 294 are expressed as intrinsic mode frequencies, or IMFs. For all variables considered, we will use a decomposition of 10
 295 IMFs, with IMF #10 being the extracted long-term trend of the time series.

296 **3.6 Analysis of Resonant Triads**

297 Resonant triad interactions are nonlinear and occur through the convective accelerations. They are described
 298 by coupled evolution equations for the “envelopes” of the three interacting waves, assumed to vary on a “slow”
 299 timescale, much longer than the actual wave periods. These non-dimensional evolution equations relate the rate of
 300 change of the complex amplitude of one wave to the product of the other two waves’ complex amplitudes (Craig,
 301 1985),

$$302 \quad (\partial_t + \mathbf{c}_j \cdot \nabla) \mathbf{Z}_j = i \delta_j (\mathbf{Z}_k^* \mathbf{Z}_l^*) \quad (9)$$

$$l \neq j \neq i$$

303 Where \mathbf{c} is the group velocity, \mathbf{Z} is the complex amplitude, \mathbf{Z}^* is the complex conjugate of \mathbf{Z} , and δ_j the interaction
304 coefficient of the j^{th} mode. The δ_j describe the strength of the wave interactions; each is the sum of a number of bilinear
305 correlations between waves. We neglect the spatial gradient terms (a “local” assumption), assume that amplitudes and
306 phases will be slowly-varying, and also assume that only one triad—the one linking the M_2 , K_1 and O_1 tides—is active.
307 Note that the triad relationships involve the slow timescale (interannual or decadal) modulations of the tidal harmonics,
308 not the fast timescale of the tidal frequencies themselves (approximately once and twice daily), and our yearly
309 admittance ratios and phase difference have already removed the fast-scale variations of the tides. Thus, our time-
310 series for AR and PD can be used to represent slow-scale variation time series of amplitudes and phases, respectively.
311 We rewrite Eq. (1) to show the form of the slowly varying complex triad modes,

$$312 \quad Z_j(\tau) = AR_j(\tau) \exp[-i(\omega_j \tau + PD_j(\tau))]. \quad (10a)$$

313 Both the AR’s and the PD’s are time-dependent, and the AR’s are real. Thus, taking the time derivative of
314 the LHS under the local assumption of Eq. (9) yields three terms,

$$315 \quad \frac{d}{d\tau}(Z_j(\tau)) = \left[\frac{dZ_j(\tau)}{d\tau} \right] Z_j(\tau) = \left[\frac{1}{AR_j(\tau)} \frac{d}{d\tau} AR_j(\tau) - i\omega_j - i \frac{d}{d\tau} PD_j(\tau) \right] Z_j(\tau). \quad (10b)$$

316 Equating this expression to the RHS, combining complex exponential terms, and separating the real and imaginary
317 terms (via the Euler formula) into two equations leads to,

$$318 \quad \left[\frac{1}{AR_j(\tau)} \frac{d}{d\tau} AR_j(\tau) \right] AR_j(\tau) = \delta_j (AR_k(\tau) AR_l(\tau)) \sin(\Phi(\tau) + \Delta\omega\tau) \quad (11a)$$

$$319 \quad \left[\omega + \frac{d}{d\tau} PD_j(\tau) \right] AR_j(\tau) = \delta_j (AR_k(\tau) AR_l(\tau)) \cos(\Phi(\tau) + \Delta\omega\tau). \quad (11b)$$

320 Here, the $\Delta\omega$ term is the sum of the frequencies as in Eq. (2b): $\Delta\omega = \omega_1 + \omega_2 + \omega_3$; for the $M_2+K_1+O_1$ triad, $\Delta\omega = 0$.
321 The $\Phi(\tau)$ term is the sum of the three phase differences: $\Phi(\tau) = PD_1(\tau) + PD_2(\tau) + PD_3(\tau)$.

322 Sets of equations like Eq. (11a; b) can, in principle, be solved using inverse scattering methods (Zakharov and
323 Manakov, 1973; Kaup, 1980), but sufficient environmental information to do so is rarely present in an oceanographic
324 context. We manipulate Eq. (11a; b), therefore, to obtain a tool for diagnosis of triad interactions; Eq. (11a) and Eq.
325 (11b) can be rewritten in terms of M_2 , K_1 , and O_1 as:

$$326 \quad C_{\text{Re}}[\text{Re}\{AR_{M_2}(\tau)\}] = \Gamma_{\text{Re}}[\text{Re}\{AR_{K_1}(\tau)AR_{O_1}(\tau)\}] \sin(\Phi(\tau)) \quad (12a)$$

$$327 \quad C_{\text{Im}}[\text{Im}\{AR_{M_2}(\tau)\}] = \Gamma_{\text{Im}}[\text{Im}\{AR_{K_1}(\tau)AR_{O_1}(\tau)\}] \cos(\Phi(\tau)) \quad (12b)$$

328 C_{Re} and C_{Im} represent the terms in brackets in Eqs. (11a,b), and $\Gamma = \Gamma_{Re} + i^*\Gamma_{Im}$ is a complex interaction coefficient
 329 related to the phase speeds and dispersion relations of the interaction. Finally, we can examine the absolute variation
 330 by combing both expressions of Eqs. (11a) and (11b) or (12a) and (12b) into a single equation,

$$331 \quad AR_{M_2}(\tau) = \frac{\Gamma_{Abs}}{C_{Abs}} AR_{K_1}(\tau) AR_{O_1}(\tau) . \quad (13)$$

332 The salient features of Eq. (13) are that: a) AR_{M_2} is proportional to the product on the RHS, and b) $\Gamma_{Abs}/C_{abs} = \beta < 0$,
 333 so that energy lost from M_2 is taken up by the two diurnals (at least if the the two diurnals behave in a similar manner).
 334 A complete triad problem requires two more equations similar to Eq. (13), but we shall only focus on the one that uses
 335 M_2 as the primary. Here, we use Eq. (13) as a diagnostic tool to identify and describe qualitatively the M_2 - K_1 - O_1 triad.
 336 Eq (2) does not use phase information. But from Eq. (2a) we have a ‘‘phase-lock’’ constraint,

$$337 \quad \Phi(\tau) = PD_1(\tau) + PD_2(\tau) + PD_3(\tau) = const. \quad (14)$$

338 For the PD variations, we convert variations from degrees to minutes. Also, β in Eq. (13) can be estimated by
 339 regressing AR_{M_2} against $AR_{K_1} \times AR_{O_1}$. Finally, triad interactions occur on slow, and possibly multiple, timescales.
 340 Thus, it is logical to compare variations on multiple scales, separated via EEMD. Trends were extracted, and modes
 341 of variability separated via EEMD, as with the thermocline data. Applying this approach, we compare the two sides
 342 of Eq. (13) using IMFs 4-10 of all quantities. To illustrate the possible importance of triad interactions, we examine
 343 below the coupled variations of M_2 , K_1 , and O_1 at Honiara and Rabaul, stations at which constituent variations are
 344 particularly strong and coherent with MSL.

345 Because the data we analyze are surface water levels and not internal wave amplitudes at the thermocline
 346 level, we cannot use Eqs. (11ab, to 13) without additional assumptions. We assume that, for nearly linear internal
 347 waves, the induced surface displacement is governed by the depth of the interface and the ratio of the restoring forces
 348 between surface and internal waves. If the changes in interfacial depth and stratification are small, then the surface
 349 displacements measured at tide gauges will be proportional to the interfacial amplitudes (and their variations)
 350 described by Eqs. (12-13). This approach allows us to analyze interactions between baroclinic and surface tides,
 351 because the surface displacements of both involve similar potential energies. The method outlined here also assumes
 352 that the wavenumber vectors for each wave are constant, with amplitudes and phases that evolve slowly. Rising MSL
 353 renders a constant wavenumber assumption questionable, especially for the vertical wavenumbers (m_i). Still, it is of
 354 interest to identify wavenumbers for which triads are possible, assuming stationary wavenumbers. For the triad of
 355 interest (K_1 , O_1 , and M_2), Eq. (2b) is exact, but Eqs. (2a), (2c) and (3) must still be satisfied. To simplify finding
 356 wavenumber vectors that satisfy the triad restraints, the dispersion relation, Eq. (3), can be recast as an aspect ratio or
 357 slope factor (Gill, 1982),

358

$$\sqrt{\frac{(\omega_i^2 - N^2)}{(f^2 - \omega_i^2)}} = \frac{m_i}{\kappa_i} \quad (15)$$

359 using a general horizontal wavenumber $\kappa_i^2 = (k_i^2 + l_i^2)$. The Coriolis frequency, f , will be dependent only on latitude,
 360 but N^2 will depend on temporally variable temperature and salinity profiles. However, because all three triad waves
 361 are present at the same place, all three will have the same N at any time. Choosing one vertical wavenumber, (m_i), κ_i
 362 is determined from Eq. (15). We then select (m_2 , κ_2 , m_3 , and κ_3) combinations that are consistent with Eq. (15) and
 363 then test their consistency with Eq. (2). Because higher modes can be involved in a resonant triad, there could be
 364 several wavenumber solutions that satisfy Eqs. (2a, c) and (3); however, higher modes are usually less energetic. We
 365 therefore only consider (vertical) modes 1 to 3, along with the zero-mode (barotropic) waves.

366 We use the Honiara and Rabaul records to illustrate the role of triad interactions in tidal evolution, because
 367 both stations show strong fluctuations in M_2 , K_1 and O_1 that are relatively coherent with MSL variations. Application
 368 of Eqs. (12-15) then requires determination of a locally appropriate density profile. N^2 profiles are estimated from
 369 temperature-salinity (T-S) profiles obtained from the World Ocean Atlas 2009: (Locarnini, et al., 2010), using the
 370 TEOS-10 (Thermodynamics Equations of Seawater) standard (Millero, et al., 2008). For convenience, we express all
 371 frequencies non-dimensionally, relative to the M_2 forcing frequency. Thus, the M_2 frequency = 1; K_1 = 0.52; O_1 =
 372 0.48. The Coriolis frequency, f , at Honiara (9.5° S), is ~ 0.17 ; that at Rabaul is ~ 0.07 . For both stations, non-
 373 dimensional N in the thermocline ranges from about 10 to 100. With these values of N , Eq. (15) can be simplified,
 374 for conceptual purposes, to:

375

$$\frac{N}{\omega_i} \cong \frac{m_i}{\kappa_i} \quad (16)$$

376 This form emphasizes the fact that K_1 and O_1 will have similar wavenumbers for any given internal wave mode.

377 Because we consider only the barotropic waves and the first three internal modes; there are only four choices
 378 for each m_i ; $m=0, 1, 2, 3$, when non-dimensionalized by depth. Inserting these values of m_i into m_i/κ_i ratio (Eqs. 15;
 379 16) gives values for the κ_i , which may be examined for conformity with wavenumber resonance condition Eq. (2c) for
 380 each mode. The vertical to horizontal aspect ratio of the ocean is small, so the $m_i \gg \kappa_i$. Because $|M_2|$ is quite small
 381 in the Solomon Sea relative to the diurnal constituents, it seems likely that the most easily detected triad is the
 382 barotropic M_2 wave interacting with a first-mode internal K_1 , and an oppositely propagating first-mode internal O_1 .
 383 This is a form of parametric sub-harmonic instability that has been analyzed in the context of a resonant triad (but not
 384 specifically the M_2 - K_1 - O_1 triad) in the South China Sea (Xie, 2008) and also near the Hawaiian Ridge (Carter and
 385 Gregg, 2006).

386 **4. Results**

387 4.1 Anomaly Trend Maps

388 The spatial distribution of anomaly trends (A-TATs and P-TATs) may help identify connections between
389 MSL rise and tidal evolution on a basin-wide, or amphidromic scale. Figures 4 to 7 show the A-TATs for each
390 constituent. P-TATs are not shown on the plots, but are discussed below in the context of possible amphidromic
391 migration. Exact values and error bands are reported in Tables 2 (A-TATs) and 3 (P-TATs). The magnitude of the
392 A-TATs is shown by the color intensity of the dots, with the color indicating positive (red) or negative (blue). For a
393 gauge with an insignificant A-TAT, the dot is white.

394 These plots provide a picture of the tidal response to a 1m MSL rise and an indication of the spatial coherence
395 of tidal evolution. For a gauge influenced by only one amphidrome, a positive (negative) A-TAT and a zero P-TAT
396 indicates that the amphidrome is moving away (towards) the gauge. Gauges that show significant P-TATs suggest a
397 rotational component to the movement of the amphidrome. If changes in tides (as represented by A-TATs and P-
398 TATs) are coherent on an amphidromic scale, they should suggest consistent amphidromic movement or rotation. If
399 statistically significant TATs do not suggest consistent amphidromic change, then local or regional process are likely
400 more important.

401 4.1.1 Diurnal Constituents

402 K_1 has its largest amplitudes along the western Pacific equator, with much lower amplitudes eastward in the
403 open-ocean (Figure 4). Based on the tidal potential, diurnal tides are expected to be small near the equator, and the
404 large amplitudes seen (4-5 times that predicted by astronomical forcing) around Indonesia and Papua New Guinea
405 may represent a resonance. Diurnal tides are larger within the Coral Sea, but are very small around New Zealand,
406 where semidiurnal tides prevail.

407 There are statistically significant ($SNR > 2.0$) positive K_1 amplitude and phase tidal anomaly trends at 18 of
408 26 gauges. Large positive A-TATs are seen at both island and shelf stations, while significant negative A-TATs are
409 only seen at island gauges. There is a concentration of positive A-TATs at Australian gauges. All negative A-TATs
410 are north of $\sim 10^\circ$ S. For the K_1 P-TATs, 18 of 26 stations are significant (though not the same 18 as the A-TATs).
411 The strongest positive P-TAT is seen at Guam, and strong negative trends in phase are seen at the islands near the
412 center of the map.

413 The amplitude and phase distributions and amphidromic patterns for O_1 are similar to those for K_1 , though
414 O_1 amplitudes are generally smaller (Figure 5). Like K_1 , O_1 is resonant near Papua New Guinea and the Indonesian
415 archipelago. Amphidromic points are again marked by “A” and “B”. Significant positive A-TATs are also found at
416 most Australian shelf stations. In total, there are 14 significant A-TATs, and 20 significant P-TATs.

417 4.1.2 Semidiurnal constituents

418 M_2 amplitudes are generally larger than diurnal amplitudes in the study area, with the largest amplitudes
419 occurring around New Zealand and the northern coast of Australia (Figure 6). An amphidromic point is located just
420 to the east of Pago Pago (marked by “B”), with an anti-node (high amplitudes) along the equator west of the date line.
421 Very low M_2 amplitudes are seen in and around the Solomon Sea.

422 There are significant M_2 A-TATs at 17 of 26 stations and significant M_2 P-TATs at 19 of 26 stations. Positive
423 and negative A-TATs are observed at both island gauges and shelf gauges. Honiara and Rabaul, which are near the
424 M_2 amphidrome in the Solomon Sea, have small mean M_2 amplitudes (~50mm), but display large relative trends; (
425 +132% for Honiara and +240% for Rabaul), though the strong phase trends at these two gauges have opposite
426 magnitudes. With the exception of Auckland, all significant positive A-TATs are south of the equator, and all negative
427 A-TATs are north of the equator.

428 S_2 is much smaller than M_2 at most locations, but with a similar (large) amplification on the northwest coast
429 of Australia (Figure 7). Also similar is the location of the amphidromic points, with “A” indicating another line-shaped
430 amphidrome (which more closely follows the Mariana trench), and an amphidromic point at “B” very near Pago Pago.

431 4.1.3 Combined Tidal Trends

432 We show the combined A-TATs in Figure 8; values and confidence limits are tabulated in Table 2. The
433 constituent TATs were combined as complex numbers (using A-TAT and P-TAT determinations for each of the four
434 constituents examined), and the real part of the result is plotted. Conceptually, a large and positive combined A-TAT
435 describes locations in which the tidal range increases strongly during periods with a positive sea-level anomaly,
436 whereas a negative combined A-TAT implies decreased tidal range for a positive MSL anomaly. Therefore, shelf-
437 locations such as Brisbane, or island stations such as Pago Pago or Noumea could see large tidal range increases for a
438 positive sea-level anomaly. By contrast, stations such as Legaspi, Guam, and Johnston could see decreased tidal range
439 for a positive sea-level anomaly. Large positive tidal-range responses are all south of 9°N, while all but one of the
440 large negative changes are north of the latitude.

441 4.2 Overtides

442 Figure 9(a-d) summarizes the spatial distribution of overtide ratios (ORs) for: M_4 , M_6 , S_4 , and MK_3 ;
443 significant long-term trends are shown as colored dots. MS_4 and MO_3 plots are shown in Figures S2 and S3 (Online
444 Resource 1). Significant changes over time for these four ORs are mainly seen at coastal shelf stations, with a few
445 islands showing some moderate change over time. The largest M_4 and M_6 ratio means are in the Solomon and Coral
446 Seas, and in general, regions of high M_4 and M_6 ratios correspond to areas where lower M_2 amplitude are found (Figure
447 6). Mean S_4 ratios are generally smaller than those for M_4 and M_6 , and fewer gauges show changes over time; those
448 that do are decreasing. Again, the S_4 ratio is large in areas where S_2 amplitudes are small (Figure 7). MK_3 is also
449 generally smaller than other overtides, but shows larger relative changes at many stations. Examination of the
450 numerators and denominators of the ORs shows that in almost all cases the trend is driven by changes in the observed

451 overtimes (numerator), not by changes in the forcing (denominator). This suggests a mechanism of changing ORs in
452 the area being driven by frictional processes rather than by secular increases or spatial shifts of the gravitationally
453 forced tides.

454 We next consider the fluctuations in ORs at Honiara and Rabaul (which show some of the largest OR values),
455 as well as the simultaneous changes in forcing tides, in MSL, and in the Multivariate El Niño Index (MEI). Figure 10
456 shows the time-series of the ORs for M_4 and M_6 ; AR amplitudes for M_2 , K_1 and O_1 ; MSL; and the MEI. These two
457 gauges show the largest ORs in the region, and very large fluctuations are associated with high values of MEI (El
458 Niño events). M_2 amplitudes are much smaller than predicted by astronomy at these gauges (~2% of gravitational
459 potential prediction), suggesting the possibility of increased relative error. However, the coherence between the two
460 records at several frequencies suggests that this is unlikely— M_2 at these two gauges show an $r^2 = 0.8$ correlation to
461 each other, M_4 overtide ratios at Honiara and Rabaul show an $r^2=0.4$ correlation to each other, and M_6 ratios have a
462 very strong $r^2=0.85$ correlation. MSL signals at the two gauges are also well correlated ($r^2=0.80$). M_4 ratios are fairly
463 well correlated to the MEI ($r^2=0.4$ for Honiara and $r^2=0.64$ for Rabaul). M_6 at Honiara shows an $r^2= 0.7$ correlation
464 to MEI, while Rabaul shows a correlation of $r^2=0.65$ for M_6 to MEI. Both gauges show very strong correlations
465 ($r^2=0.85$ for Honiara; $r^2 = 0.75$ for Rabaul) of local MSL to the MEI.

466 Figure 9 suggests that there is a threshold relationship between the occurrence of large ORs, local MSL, and
467 the MEI. As shown by the yellow boxes, significant increases in ORs by a factor of $3\times$ to $10\times$ occur when the MEI
468 is high and MSL is low, under El Niño conditions. Increased OR values during El Niño periods of low MSL could
469 result from several factors, including increased friction over reefs and in shallow lagoonal areas. Most of Indonesia
470 and Australia receive less rain during El Niño events (Roplewski and Halpert, 1987, Figure 21). Honiara and Rabaul
471 are on the edge of this ENSO-induced drought region, and MSL rapidly decreases at both these gauges during El Niño
472 events. M_4 and M_6 ORs have started to decrease in recent years at Honiara, while M_2 has shown a strong increase.
473 This is likely due to the fact that sea level has risen rapidly in recent years, reducing bed friction.

474 **4.3 Thermocline depth and tidal variations**

475 Thermocline depth, MSL and tidal properties are closely linked at some, but not all, stations. Figure 11 shows
476 EEMD decomposed time-series (seasonal scales and longer) of D_{20} from the TAO buoys (as detailed in section 3.5),
477 along with the M_2 and S_2 tidal amplitude variations (determined from monthly admittance amplitudes); for all relevant
478 time series, we only use IMFs #4-9 so the long-term trends are not included. This analysis is performed at Honiara,
479 Kapingamarangi, and Pago Pago; buoys and gauge locations are shown in Figure 11a. The D_{20} variations at the three
480 TAO buoys nearest Honiara are mutually coherent; we take, therefore, a mean of these three equidistant buoys (Figure
481 11b). For the other two gauges, only one TAO buoy is used to compare thermocline depths. Figure 11c and 11d show
482 this D_{20} time-series with M_2 and S_2 variations at Honiara and Kapingamarangi; both gauges show positive correlations
483 of thermocline depth fluctuations to M_2 and S_2 fluctuations, with r^2 being between + 0.69 and + 0.89 in all cases. For
484 Pago Pago, the coherence between the time-series is insignificant ($r^2 < 0.1$). It is unclear whether this is the result of

485 the distance between buoy 5 and Pago Pago, or whether different processes are at work at this station. The thermocline,
486 as represented by D_{20} , shoaled during the 1997-1998 ENSO event. At the same time, there was drop in tidal admittance
487 for M_2 and S_2 at Honiara, Kapingamarangi, and Pago Pago, but available data do not provide any apparent connection
488 of the tides to changes in thermocline depth at Pago Pago.

489 **4.4 Spatial Summary**

490 The long-term trends of the M_2 tide are mainly positive, while diurnals are mixed, but generally negative, in
491 Australian and New Zealand waters. For the A-TATs, M_2 is mainly negative, while the diurnal A-TATs are all
492 positive. Overtides, even M_4 , are generally growing, despite extensive harbor development at some locations. These
493 changes suggest regionally driven tidal evolution involving a combination of frictional and triad interaction, perhaps
494 tied to the reef systems in the Coral Sea. The waters around the Solomon Islands show M_2 A-TAT to be increasing,
495 while K_1 , O_1 and the main overtide ratios are decreasing, with all variations coherent with, and likely driven by,
496 variations in the depth of the thermocline.

497 **4.5 Anomaly Trends Over Time**

498 The majority of the Western Pacific stations used in this study show larger yearly MSL rise rates after 1993
499 than before (Table 1a; Figure 2). This rather abrupt increase in MSL rise in the southwest Pacific after 1993 provides
500 an opportunity to test the relationship between MSL rise and tidal evolution. Thus, if TATs are sensitive to absolute
501 MSL or rate of change of MSL, we might expect to see differences in TATs between these two epochs at gauges that
502 show MSL acceleration. If TATs are the same in both time periods for such gauges, then they are likely independent
503 of MSL. Thus, analyses were performed to evaluate differences in TATs before and after 1993. Twenty out of 26
504 stations have enough data both before and after 1993 to cover a nodal period and allow meaningful comparison.
505 Results of the “before and after” 1993 analyses for these 20 gauges are summarized in Tables S1 (K_1) and S2 (M_2)
506 (Online Resource 1). To illustrate spatial trends in these shifts, figures are provided for K_1 (Figure 12) and M_2 (Figure
507 13), analogous to Figure 4 through 7, but now the color intensity of the dots represent the *difference* in A-TATs
508 between the two time eras.

509 There are strong positive K_1 A-TAT temporal shifts at three shelf gauges, and at two islands; there is a
510 negative shifts at only one shelf gauge. M_2 A-TAT shifts tend to be generally larger than K_1 . Most shelf gauges show
511 significant M_2 shifts, positive at four, and negative at two stations. Two island gauges show positive shifts, with only
512 one negative result. In general, shelf gauges show larger magnitude shifts than island gauges, where it is harder to
513 distinguish the two periods (pre and post-1993). Similar plots and tables are provided for O_1 (Figure S4, Table S1,
514 Online Resource 1) and S_2 (Figure S5, Table S2, Online Resource 1). O_1 A-TATs shifts are also mainly positive after
515 1993, but S_2 A-TATs and P-TATs have shifted only slightly.

516 **4.6 Triad Results**

517 The Honiara and Rabaul tidal records show striking examples of what appears to be M_2 - K_1 - O_1 triad
518 interactions (Figures 14 and 15). Figure 14 (a) shows K_1O_1 vs. M_2 at Honiara; Figure 14(b) shows Rabaul. M_2
519 amplitudes are small, 51mm at Honiara and 40 mm at Rabaul, and their temporal variability is high (Figures 10 and
520 11). Diurnal tides are larger; K_1 amplitudes are 229mm and 240mm at Honiara and Rabaul, while O_1 amplitudes are
521 112mm and 126mm, respectively. Since we further multiply the K_1 and O_1 ARs together, the magnitude of the RHS
522 of Eq. (13) will be much larger than the M_2 AR appearing on the LHS, meaning that the interaction coefficients, β ,
523 must be small as well as negative (Figure 14). As noted above, β can be estimated by regression, using Eq. (13); see
524 Figure 15. If triad resonance is occurring, the variations of the summed variables (LHS and RHS sides of Eq. (13))
525 should be less than the variations in the LHS and RHS individually, a condition that is generally fulfilled for both
526 stations in Figure 14, though some deviations are seen during El Niño. Also, the r^2 values of 0.59 (Honiara) and 0.72
527 (Rabaul) in Figure 15 suggest that resonant triad dynamics explain a substantial fraction, though not all, of the
528 variations in the major constituents at these stations. A fraction of this energy may be lost to overtide generation
529 during El Niño events, but direct comparison of M_4 and M_2^2 fluctuations does not show a significant correlation.
530 Finally, the variations in AR_{M_2} are impressive: $\pm 30\%$. Thus for a small constituent like M_2 , triad interactions can
531 lead to very large time variations, in relative terms.

532 Also, it is evident from Figure 16 and Table 4 that the phase-lock condition Eq. (2a) is generally
533 approximately met for IMF#s 4-10. While $\Phi(\tau)$ is not constant, particularly during the ENSO events, it is less variable
534 than the individual phases. For most of the record, the O_1 and K_1 PDs are negatively correlated, with M_2 making up
535 the difference between the two. During El Niño events, in contrast, there are large M_2 phase excursions that perturb
536 the phase lock. The sum of the variances is 2-13 \times as large as the variance Φ , and the phase lock is more closely met
537 after 1993 than before, despite very large fluctuations in the O_1 PD. Interestingly, the 1998 El Niño does not cause
538 large excursions in the M_2 PD, even though large M_4 amplitudes are seen at Honiara.

539 To confirm that the variations shown in Figures 14-16 indeed represent a triad interaction, we should verify
540 that the resonance conditions of Eq. (2) and Eq. (3) are satisfied. For M_2 , K_1 , and O_1 , the frequency condition, Eq.
541 (2b), is satisfied by definition, and the phase-lock condition, Eq. (2a), is shown in Figure 15. There are, however, only
542 a few wave combinations that will satisfy the resonance condition, Eq. (2c), that $\Sigma \mathbf{k}_i = 0$. For simplicity, we consider
543 only cases in which Eq. (2c) can be satisfied in two dimensions (2D). We exclude 3D solutions on the grounds that
544 they would require a rather special geometry and that the matching conditions would likely be transient -- small
545 changes in thermocline depth could cause large changes in the angles between the matching wavenumber vectors.
546 Given fixed geometry, it seems unlikely that the resonance would endure. There are only two possible 2D interactions
547 between waves of zero or low vertical wavenumber. The most likely situation is a parametric sub-harmonic instability
548 (PSI): a barotropic M_2 wave interacting with first-mode K_1 and O_1 internal waves. The other possibility is a second
549 mode M_2 wave interacting with first and third mode diurnal waves, the case examined numerically by Lamb (2007).

550 For the PSI case, the vertical wavenumber for M_2 is $m_{M_2}=0$; and κ_{M_2} will be small relative to the κ_i for the
551 diurnals, because barotropic tidal wavelengths are much longer than internal wavelengths. As detailed above, we find

552 values of the m_i/κ_i ratio for the internal waves from Eq. (11). Table 5a shows these ratios for a range of values of N
553 of 10-100. The m_i for K_1 and O_1 will be equal and of opposite sign, while their κ_i will differ by $\sim 8\%$. An exact triad
554 would occur when the small difference between the two diurnal κ_i matches the κ_{M_2} . For the barotropic forcing wave,
555 M_2 , we find κ from the shallow-water relation: $\kappa = \omega/\sqrt{gH}$, where g is the gravitational acceleration, ω is the
556 frequency of M_2 , and H is the bottom depth, taken to be $\sim 500\text{m}$ based on the average depth near Honiara. These values
557 yield a $\kappa = 2.0 \times 10^{-6} \text{ m}^{-1}$. However, the depth in this area is highly variable and water depths of up to 5km are found
558 within a wavelength of Honiara. If, on the other hand, the triad interaction is localized near the gauge, the relevant
559 depth could be as little as $100\text{-}200\text{m}$. Thus, a plausible range of κ values for barotropic M_2 is ~ 0.7 to $4 \times 10^{-6} \text{ m}^{-1}$. For
560 the K_1 and O_1 first-mode internal waves, the internal wave relation gives $\kappa = \omega/c_{\text{ph}}$, where c_{ph} is the phase speed of
561 each wave. We use the N profile near Honiara (with $10 < N < 100$) to find a typical first-mode diurnal $c_{\text{ph}} \sim 2.7 \pm 0.1 \text{ ms}^{-1}$
562 for both K_1 and O_1 (Rainville and Pinkel, 2006). The resulting first-mode wavenumbers are: $\kappa \sim 2.7$ and $2.5 \times 10^{-5} \text{ m}^{-1}$
563 for K_1 and O_1 , respectively. The difference between these two κ values, $\sim 2 \times 10^{-6} \text{ m}^{-1}$, gives an exact resonant triad ($\Delta\kappa$
564 $= 0$) for a barotropic M_2 wave corresponding to depth of 500m , as well as near-resonant triads for depths ranging from
565 5000 to 100m (Table 5b). Given the uncertainty in and temporal variability of N , an exact resonant triad is likely
566 present only on a transient basis, and a near-resonant triad is probably the usual situation. It is encouraging, however,
567 that such a simple configuration is possible in 2D, and Table 5b indicates that $\Delta\kappa$ remains small for a range of possible
568 values of N .

569 There is only one 2D, low-mode M_2 - K_1 - O_1 triad that does not involve a barotropic wave: 1st ($m = \pm 1$) and 2nd
570 mode ($m = \pm 2$) waves of the same sign, coupled with a 3rd mode wave ($m = \mp 3$) of opposite sign. To satisfy the
571 wavenumber condition Eq. (2c), the second mode wave must be M_2 , the case studied by Lamb (2007). There are two
572 "flavors" of this triad, because there are two diurnals (K_1 and O_1), one third mode and one first mode. Which diurnal
573 should be chosen as the first mode depends on the fit to Eq. (2c) -- the correct choice will minimize $\Delta\kappa$. Table 5c lists
574 the κ_i and $\Delta\kappa$ for these two possibilities. $\Delta\kappa$ is minimized by factor of 5 for a K_1 mode 3 and an O_1 mode 1 over the
575 reverse situation, but both show a very small $\Delta\kappa$. While both the Lamb analysis and Table 5c suggest that this triad is
576 possible, measurable surface deflections seem unlikely for an M_2 wave with $m = \pm 2$, given the small barotropic M_2 in
577 the Solomon Sea. Thus, it seems a less likely candidate to account for the triad features seen in Figures 14-16.

578 **5. Discussion**

579 We observed above that fluctuations in observed tidal properties are associated with sea-level anomalies. At
580 three stations (Honiara, Kapingamarangi, and Rabaul), semidiurnal tidal properties (influenced by both local and
581 amphidromic scale processes) and overtide generation (a local, frictional process) are strongly correlated with
582 anomalies in sea level and stratification. These observations leave open, however, the question of whether constituent
583 variability is primarily related to local processes, to basin-scale phenomena, or to some combination thereof.
584 Furthermore, it is yet to be determined if the observed tidal variability is influenced only at the at the interannual time

585 scale, or if there is also a combination of dynamics across multiple frequency bands, including the long-term trends
586 of MSL. In the following discussion we attempt to identify the mechanisms behind the observed TATs.

587 **5.1 Spatial Patterns**

588 Here we summarize and interpret spatial patterns in selected areas, focusing on two regions that exhibit
589 reasonably coherent changes; a) the eastern coast of Australia and the Great Barrier Reef; and b) the Solomon Sea.
590 We will also consider not just the anomaly trends (TATs), but also the long term trends (LTTs) in tidal constituents.

591 *5.1.1 Australian Shelf and the Great Barrier Reef*

592 Anomaly trends for the Australian stations are relatively coherent. There is a positive trend in the A-TATs
593 for K_1 and O_1 along the eastern Australian coast, and (with the exception of Brisbane) a negative trend to M_2 A-TATs.
594 Stations north of Brisbane lie on the semi-enclosed Coral Sea behind the Great Barrier Reef (GBF); the regional
595 bathymetry is highly variable, from deep (>4000m) to inter-tidal. The pattern of TATs suggests larger diurnal and
596 smaller semidiurnal tides in this region as MSL rises. The large trends in A-TATs at Auckland show a heightened
597 sensitivity of tidal dynamics to water level, though New Zealand has its own M_2 amphidrome, the dynamics are still
598 likely connected to the Australian waters across the Coral Sea. Auckland shows a negative M_2 A-TAT and a negative
599 LTT in M_2 , but for diurnals the A-TAT is positive and the LTT negative.

600 Overtide ratios (Figure 9) for M_4 and MK_3 are increasing for most Australian stations north of Brisbane, with
601 some of the largest increases seen at Cairns (+3%yr⁻¹ for M_4 , and +4%yr⁻¹ for MK_3). Decreases are seen only at
602 Townsville for S_4 and MK_3 (-2%yr⁻¹) and at Bundaberg and Gladstone for M_4 (-2%yr⁻¹). Overtides are typically driven
603 by frictional interactions, and friction at harbor stations is usually reduced, not increased, by navigational development
604 (e.g., Jay et al., 2011), which may help explain the decreasing trends at Townsville, Bundaberg, and Gladstone. These
605 harbors are amongst the busiest in Australia, and have had an extensive history of development over the last 50 years.
606 This would not, however, explain the overtide increases seen at other nearby Australian gauges. It is likely that the
607 regional overtide changes are related to larger scale processes, perhaps a coupling of resonant triads and overtides.
608 Tidal evolution at the Australian gauges on the Coral Sea may be a response in part to MSL rise over the complex
609 topography of the Great Barrier and other reef systems (Hughes, et al, 2010; Hughes et al, 2003; Wolanski, 1994).

610 *5.1.2. Solomon Islands: Overtide Ratios and Thermocline Depth Variations*

611 The Honiara and Rabaul tide gauges are located in an area of water shallower (~300-700m) than at nearby
612 island stations. To the direct west of the island chain is the deep Solomon Sea basin, which is connected to the waters
613 of Honiara and Rabaul via a semi-enclosed basin directly east of Papua New Guinea known as “The Slot”. Much
614 deeper water lies both north and south of Honiara and Rabaul, but the only open-water connection to the north is a
615 through a narrow deep channel east of the Honiara gauge. The connecting waters south of Honiara and Rabaul have
616 very strong currents due to the motion of the South Equatorial Current (SEC) that runs through the area, both on the
617 surface, and in the deeper thermocline layer. The local bathymetry (Figure 1) is irregular and steep, with relatively

618 narrow deep-water connections between neighboring deep-water basins. This region also has some of the strongest
619 ORs for M_4 , and M_6 , an order of magnitude greater than neighboring stations. The connections detailed above between
620 the temporal fluctuations in the ORs, MSL and the El Niño (Figure 10) highlight the heightened sensitivity of tides to
621 water level in this area. Thus, changes in friction, related to changes in lagoonal inundation or “sill depth” that connect
622 the deep and interconnecting basins in the complex bathymetric region may be tied to changing ORs, since the large
623 MSL fluctuations due to ENSO represent a larger relative change in water level. The M_2 A-TAT is positive at Honiara
624 and Rabaul, while the both the diurnals show negative A-TATs. Long-term trends are negative at Honiara for M_2 , K_1 ,
625 and O_1 . At Rabaul, the long-term trends are negative in M_2 and positive for the diurnals, but this trend is only estimated
626 up to 1997 when the Rabaul gauge was de-commissioned so a direct comparisons of LTTs will not be accurate.

627 The similarity of behavior between TATs and D_{20} variations (Figure 11) suggests that the semidiurnal tidal
628 properties in this region may be dependent on local thermocline depth. These results are (at least partially) consistent
629 with the processes inferred for Hawaii; i.e., that increased M_2 amplitude is correlated with times of deeper thermocline,
630 due to changing internal wave phases (Mitchum and Chiswell, 2000; Colosi and Munk, 2006). In principle, changing
631 thermocline depth could change ORs by altering internal tidal wave steepness. However, the observation (above) that
632 changes in ORs are driven by changes in the overtides (not the parent constituents) suggests a frictional mechanism.
633 That is, it seems unlikely that the M_2 wave would become significantly steeper at several stations without modifying
634 M_2 amplitudes at any of them. Moreover, the deeper thermocline during El Niño does not suggest internal tide
635 steepening. Finally, scaling relationships suggest that changes in friction associated with lowered sea levels are a more
636 likely cause of increased ORs than internal wave steepening. In any event, evidence for a direct relationship between
637 overtides, the thermocline, local MSL and the forcing tides can only so far be provided for the gauges near the Solomon
638 Islands (Rabaul, Honiara, Kapingamarangi), presumably due in part to the variable topography and shallower relative
639 water level amplifying both the overtide and thermocline mechanisms. However, lack of correlation between ORs and
640 thermocline depth may also be attributable to the distance of the TAO buoy datasets from other gauges in the study
641 area, e.g., near Pago Pago.

642 **5.2 Temporal changes**

643 Analyses of TATs before and after 1993 show that most stations on the Australian shelf exhibit larger A-
644 TATs before than after 1993 for M_2 , and also for K_1 (Figure 12 and 13; Tables S1 and S2; Online Resource 1). No
645 other region in this study showed such spatial coherence in the shifting of TATs. Overall, these results are locally
646 interesting, but do not conclusively show that the rate of MSL during different epochs is directly influencing the
647 response of the tides to MSL variability, since the majority of all gauges analyzed show more or less unchanged TATs
648 before 1993 and after. Gauges that do show a significant shift in TATs are likely due to local dynamical factors
649 mentioned above (overtide and thermocline variability), as well as the fact that the post-1993 period captures the 1997-
650 1998 El Niño event, the strongest such event in the modern record, which produced the largest interannual variability
651 in both MSL and the tidal dynamics, particularly in this region. Therefore, the comparison of the tidal variability

652 between these two time periods with different MSL rates is either not able to isolate the effect of long-term sea level
653 change, or it is not the mechanism for the observed tidal variability at this time scale.

654 **5.3 Amphidromic movements**

655 The observed TATs for K_1 (Figure 4) are consistent with a westward, slightly northwest-ward movement and
656 counter-clockwise rotation of amphidrome “A”, and an eastward movement and clockwise rotation of amphidrome
657 “B” associated with positive MSL fluctuations. These combined motions would also allow an increase in the K_1
658 amplitudes within the Coral Sea, as observed in TATs for the area. Though diurnal A-TATs are decreasing at nearby
659 Honiara and Rabaul, these gauges are within a semi-enclosed basin, and are essentially separated from the Coral Sea
660 and the open Pacific. The O_1 tidal field shows a similar movement of amphidromic points as K_1 (Figure 5) Unlike K_1 ,
661 there is an additional amphidromic point off the New Zealand coast. A westward movement of this point would
662 explain trends observed at the Australian shelf and Auckland. Thus, we conclude that changes in diurnal tides within
663 amphidromes “A” and “B” are amphidromic scale, though modulated by other local factors at some stations.

664 For M_2 , (Figure 6) an eastward movement of amphidrome “B”, along with a counterclockwise rotation that
665 expands anti-node “C” westward and southwest-ward would agree with most of the observed M_2 TATs. The long,
666 narrow amphidrome, “A” (more or less aligned with the Mariana Trench) is not changing in an obvious pattern. The
667 S_2 patterns (Figure 7) of A-TATs and P-TATs show some similarities to those for M_2 (e.g., at Yap, Kapingamarangi,
668 and Noumea), but also many differences (e.g., Legaspi, Rabaul and Pago Pago). Honiara has a similar M_2 A-TAT to
669 other regional gauges, but an opposite P-TAT. The overall pattern of change for S_2 may echo M_2 , with an amphidromic
670 point east of Pago Pago moving westward, and a central anti-node rotating counter-clockwise. It is not surprising that
671 the M_2 and S_2 behavior show some difference, because S_2 has a significant radiational component that is absent for
672 M_2 (Godin, 1986; Ray, 2001; Arbic, 2005). Still there is a strong suggestion of regional coherence for the semidiurnals,
673 as with the diurnals.

674 If these suggestions of amphidromic-scale tidal evolution are real, they require an explanation relevant to
675 such a scale. The two most likely candidates are the barotropic “back-effect” mechanism suggested by Arbic and
676 Garrett (2010) and altered stratification (Müller, 2012). The first requires continental shelf areas over which friction
677 or depth are changing, which seems more relevant to amphidrome B, for both the diurnals and the semidiurnals.
678 Altered stratification may have occurred over large areas in both amphidromes A and B, and there is a clear connection
679 between stratification and tidal properties at Honiara and Kapingamarangi. At least the latter is affected by
680 amphidrome A for both diurnals and semidiurnals. Thus altered stratification seems the more likely agent of tidal
681 evolution in amphidrome A. We note that amphidromic movements are not a cause of the observed TATs, but are
682 rather symptoms of tidal evolution that represent a re-distribution the tidal fields driven by other factors.

683 **5.4 Triad Interactions**

684 Honiara and Rabaul in the Solomon Sea show resonant triad behavior at sub-decadal and longer timescales,
685 with some fluctuations during ENSO events. Estimates of possible wave vectors show there are multiple situations
686 that can satisfy the resonance conditions, Eqs. (2) and (3). Triads that involve higher- mode internal tides are, however,
687 unlikely to be observed at a coastal tide gauge. Thus, the triad interaction that we do see is possibly a parametric
688 subharmonic instability (PSI) interaction of barotropic M_2 with first-mode internal K_1 and O_1 .

689 There are also frictional triad interactions in the Solomon Sea that are correlated with MSL fluctuations,
690 likely due to decreased lagoonal depths during periods of lowered MSL (Figure 10). Thus, frictionally-driven
691 overtides M_4 and M_6 strongly vary with MSL (and thermocline depth) even though MO_3 and MK_3 do not. This likely
692 reflects the fact that M_2 is decreased and the diurnals (K_1 and O_1) increased by a deeper thermocline. These opposite
693 fluctuations compensate each other in MO_3 and MK_3 , while M_4 and M_6 variations are proportional to the square and
694 cube (respectively) of M_2 . Interestingly, the strong ENSO events, which caused large fluctuations in MSL, O_1 , K_1 ,
695 M_2 , M_4 , and M_6 individually, do not destroy the triad conservation relation Eq. (14), because of the manner in which
696 the oscillations in individual constituents are coupled.

697 Resonant triad behavior at Honiara shows a difference in behavior before and after 1993, with larger
698 excursions from stability after 1993. These excursions are caused by decreases in K_1 and O_1 amplitudes that are not
699 fully compensated by changes in M_2 . These may be caused by the rising MSL in the area. Also, the ENSO response
700 in 2009 and 2010 was less dramatic than in the four previous El Niños, perhaps because the most recent El Niño was
701 weaker. Determining whether MSL rise has fundamentally altered Solomon Sea triad behavior awaits the next major
702 El Niño.

703 **6. Conclusions**

704 Tidal anomalies are related to MSL anomalies via tidal anomaly trends for both amplitude and phase (A-
705 TATs and P-TATs) over much of the western Tropical Pacific, at both coastal and open-ocean stations. Comparison
706 of periods before and after 1993 at stations with records >40 yrs long shows considerable temporal variability. .
707 However, complex spatial patterns, differences between constituents and differences between TATs and trends make
708 it difficult to draw conclusions regarding causes of tidal evolution. Observed trends so far suggest the existence of
709 multiple mechanisms with spatial scales from strictly local (e.g., lagoonal depth and harbor modification) to
710 amphidromal, as evidenced in the apparent movement and rotation of both diurnal and semidiurnal amphidromes.
711 Comparison of the long-term trends (LTTs) in MSL and tidal properties with the short-term variability of MSL and
712 tides, as exhibited by the A-TATs and P-TATs, do not show ubiquitous overlap of behavior. At some locations, the
713 LTTs and TATs are correlated, but at others, anti-correlated. This suggests that multiple dynamics are active in
714 different parts of the frequency spectrum, with temporal scales from interannual to decadal, and as of yet, no significant
715 prediction about the future behavior of tidal constituents may be inferred from the analysis of interannual tidal and
716 MSL fluctuations. Thus, the question posed in the title must be answered in the negative, at least for now, though
717 further analysis with longer records from a different part of the world ocean might suggest a different answer.

718 Two regions were studied in detail; the Solomon Sea, and the Coral Sea area including the east coast of
719 Australia and New Zealand. Both areas show regionally coherent changes, but with different manifestations. In both
720 cases, there is considerable variability between stations related to local processes. To the extent that the reefs of the
721 Coral Sea are a factor, changes in the Australia-New Zealand area may be unusual – regionally coherent but not likely
722 applicable in other settings.

723 To summarize the available evidence:

- 724 1. Internal tides: The surface manifestation of internal tides, generated across steep topography, can affect major
725 tidal constituents over the entire region investigated here, which is between the critical latitudes for both diurnal
726 and semidiurnal tides. There has been a deepening and strengthening of the thermocline in the area (documented
727 for 1993-2003 by Church et al., 2011), which necessarily changes internal tides and may affect surface tides
728 (Müller, 2012). The M_2 and S_2 constituents are strongly (positively) correlated with nearby thermocline depth in
729 the region surrounding the Solomon Islands as well as MSL, and diurnal tides show a negative (decreasing)
730 response to increasing MSL and deepening thermocline. Thus, changing stratification appears to be the most
731 likely agent of large-scale tidal evolution in the northern part of the study area (amphidrome A for both diurnals
732 and semidiurnal). It may affect amphidrome B in the southern part of the study area, but we have no definite
733 evidence of this.
- 734 2. Changing friction: Frictional interactions are most prominent for overtides but affect the main tidal species as
735 well. A-TATs, and LTTs of the major tides sometimes reinforce each other, but also show opposing behavior at
736 some locations. These two calculations of trends have different time scales, and are likely due to unrelated
737 mechanisms. The similarity in trends between coastal and island stations gives some support to the hypothesis
738 that changes in amphidrome B may be driven by continental shelf processes, which can have a back-effect upon
739 open-ocean trends (Arbic and Garrett, 2010). Comparison of TATs for the pre- and post-1993 periods shows the
740 trends have changed for many Australian shelf stations, including sign reversals. Changes in ORs over time also
741 suggest a frictional component to changing tides in the region of study. Particularly over the Australian shelf, this
742 appears to have a regional rather than local origin.
- 743 3. Resonant triad interactions: Triad interactions of the diurnal and semidiurnal tides (K_1 , O_1 , and M_2), may both be
744 mediated by and enhanced by variations in thermocline properties (Ball, 1964). The strength of these interactions
745 can be modulated by changing water depth (MSL), which changes bottom friction, and also the deepening of the
746 thermocline, which changes both surface-layer depth and stratification. Triads can involve a transfer of tidal
747 energy across multiple frequencies, and is therefore a likely candidate to connect the other variability explored in
748 this work, as illustrated by analysis of the Honiara and Rabual in the Solomon Sea region. Whether triad
749 interactions are relevant on a regional basis, or only locally important, remains unclear.

750 It is likely the above mechanisms are not altogether independent, and the situation in the Solomon Sea
751 suggests that there is a connection between triad and frictional interactions, with M_2 energy feeding both the resonant

752 and frictional triads. This results in large ($\pm 30\%$) interannual fluctuations in M_2 amplitude. Variations in thermocline
753 depth may be tied to changes in shallow water frictional interactions, because a shallower total depth makes
754 fluctuations in the upper-layer thickness larger, in percentage terms, than at deep water stations. The amphidromic
755 movements associated with MSL will likely have secondary regional effects as the basin-wide water levels and tidal
756 admittances adjust to changes in sea level and in thermocline profile. Resonant triads may also help redistribute the
757 amphidromes of each wave involved in the triad. Further work is underway to test the contribution of each of these
758 mechanisms through modeling in coordination with analyses of satellite altimetry data, as well as investigations
759 focusing on sub-annual (seasonal) dynamics based on complete monthly analyses.

760

761 **Acknowledgements:** Support for this project was provided by the National Science Foundation (NSF) project: Secular
762 Changes in Pacific Tides, OCE-0929055, and by the National Aeronautics and Space Administration (NASA) project:
763 NNX13AH06G. Thanks to Land Information New Zealand (LINZ) and Glen Rowe who provided data for Auckland
764 after extended personal communication.

765

766

767 **References:**

- 768 Arbic BK, Karsten RH, Garrett C (2009) On tidal resonance in the global ocean and the back-effect of coastal tides
769 upon open-ocean tides, *Atmosphere-Ocean* 47 (4) , 239–266, DOI:10.3137/OC311.2009
- 770 Arbic BK and Garrett C (2010) A coupled oscillator model of shelf and ocean tides *Cont. Shelf Res.* 30 (6), 564-574,
771 DOI: 10.1016/j.csr.2009.07.008
- 772 Arbic BK (2005) Atmospheric forcing of the oceanic semidiurnal tide, *Geophys. Res. Lett.*, 32, L02610,
773 DOI: 10.1029/2004GL021668
- 774 Armstrong JA, Bloembergen N, Ducuing J, Pershan PS (1962) Interactions between light waves in a nonlinear
775 dielectric, *Phys. Rev.* 127, 1918-1939, DOI: 10.1103/PhysRev.127.1918
- 776 Ball FK (1964) Energy transfer between external and internal gravity waves, *J. Fluid. Mech.*, 20, 465-478, DOI:
777 10.1017/S0022112064001550
- 778 National Research Council (2012) *Sea-Level Rise for the Coasts of California, Oregon, and Washington: Past,*
779 *Present, and Future.* National Academies Press
- 780 Bretherton FP (1964) Resonant interactions between waves *J. Fluid Mech.*, 20, 457-479, DOI:
781 10.1017/S0022112064001355
- 782 Bromirski PD, Miller AJ, Flick RE, Auad G (2011) Dynamical suppression of sea level rise along the Pacific coast
783 of North America: Indications for imminent acceleration., *Jour. Of GeoPhys. Res.* 116, CO7005,
784 DOI: 10.1029/2010JC006759
- 785 Carter GS, Gregg MC (2006) Persistent near-diurnal internal waves observed above a site of M₂ barotropic-to-
786 baroclinic conversion, *Jour. of phys. Oceanogr.* 36(6), 1136-1147, DOI: 10.1175/JPO2884.1
- 787 Cartwright DE, Edden AC (1973) Corrected tables of tidal harmonics *Geophys. Res. Lett.* 33, 253-264,
788 DOI: 10.1111/j.1365-246X.1973.tb03420.x
- 789 Cartwright DE, Tayler RJ (1971) New computations of the tide-generating potential, *Geophysical Journal of the Royal*
790 *Astronomical Society*, 23, 45-74, DOI: 10.1111/j.1365-246X.1971.tb01803.x
- 791 Cazenave A, Nerem RS (2004) Present-day sea level change: observations and causes, *Reviews of Geophysics*, 42,
792 RG3001, 1-20, DOI: 10.1029/2003RG000139
- 793 Chiswell, SM (1994) Vertical structure of the baroclinic tides in the central North Pacific subtropical gyre, *Jour. Of*
794 *Phys. Oceanogr.* 24, 2032-2039, DOI: 10.1175/1520-0485(1994)24[2032:VSOTBT] 2.0.CO;2
- 795 Church JA and White NJ (2006) A 20th century acceleration in global sea-level rise, *Geophys. Res. Lett.*, 33, L01602,
796 DOI: 10.1029/2005GL024826

797 Church, JA and White, NJ (2011) Sea-Level Rise from the Late 19th to the Early 21st Century. *Surv. Geophys.*, DOI
798 10.1007/s10712-011-9119-1

799 Church JA, Roemmich D, Domingues CM, Willis JK, White NJ, Gilson JE, Stammer D, Köhl A, Chambers DP,
800 Landerer FW, Marotzke J, Gregory JM, Tatsuo Suzuki, Cazenave A, Pi.-Y. Le Traon, (2011) Ocean
801 Temperature and Salinity Contributions to Global and Regional Sea-Level Change, in *Understanding Sea-Level*
802 *Rise and Variability*, Wiley-Blackwell, Oxford, pp. 143-176, DOI: 10.1029/2007EO040008

803 Church JA, White NJ, Coleman R, Layback K, Mitrovica JX (2004) Estimates of the regional distribution of sea level
804 rise over the 1950-2000 period, *J. Clim.*, 17, 2609-2625, doi:10.1175/1520-0442(2004)

805 Colossi JA and Munk W (2006) Tales of the Venerable Honolulu Tide Gauge, *J. Phys. Oceanogr.*, 36, 967–996, DOI:
806 10.1175/JPO2876.1

807 Craik, A. D. D. (1985) *Wave Interactions and Fluid Flows*, Cambridge Univ. Press, Cambridge, U. K, ISBN: 978-
808 0521368292

809 Domingues CM, Church JA, White NJ, Glecker PJ, Wijffels SE, Barker PM, Dunn JR (2008) Improved estimates
810 of upper-ocean warming and multi-decadal sea-level rise, *Nature*, 453, 1090-1094, DOI: :10.1038/nature07080

811 Dushaw BD, Cornuelle BD, Worcester PF, Howe BM, Luther DS (1995) Barotropic and baroclinic tides in the central
812 North Pacific Ocean determined from long-range reciprocal acoustic transmissions, *Jour. Of Phys. Oceanogr.* 25,
813 631-647, DOI: 10.1175/1520-0485(1995)025<0631:BABTIT>2.0.CO;2

814 Egbert GD and Erofeeva SY (2002) Efficient inverse modeling of Barotropic Ocean tides, *J. Atm. and Ocean. Tech.*,
815 19, 18 (204), DOI: 10.1175/1520-0426(2002)019<0183:EIMOBO>2.0.CO;2

816 Egbert GD and Erofeeva SY (2010) OTIS (OSU Tidal Inversion Software) TPXO7.2. College of Oceanic and
817 Atmospheric Sciences, Oregon State University, Corvallis, Oregon, <http://volkov.oce.orst.edu/tides/otis.html>

818 Flick RE, Murray JF, Ewing LC (2003) Trends in United States Tidal Datum Statistics and Tide Range, *J. Waterway,*
819 *Port, Coastal and Ocean Eng.* Amer. Soc. Civil Eng., 129(4): 155–164, DOI: 10.1061/~ASCE10733-
820 950X~20031129:4~1551

821 Gerkema, T., C. Staquet, and P. Bouruet-Aubertot (2006) Decay of semidiurnal internal-tide beams due to
822 subharmonic resonance, *Geophys. Res. Lett.*, 33, L08604, DOI: 10.1029/2005GL025105

823 Gill, AE (1982) *Atmosphere-ocean dynamics* (Vol. 30), Academic press, ISBN: 978-0122835223

824 Haigh I, Nicholls R, Wells N (2010) Assessing changes in extreme sea levels: Applications to the English Channel,
825 1900-2006, *Cont. Sh. Res.* 30, 1042-1055, DOI: 10.1016/j.csr.2010.02.002

826 Hamlington, BD, Leben RR, Nerem W, Han K, Kim KY (2011) Reconstructing sea level using cyclostationary
827 empirical orthogonal functions, *J. Geophys. Res.*, 116, C12015, doi:10.1029/2011JC007529

- 828 Hibiya, T., M. Nagasawa, and Y. Niwa (2002) Nonlinear energy transfer within the oceanic internal wave spectrum
829 at mid and high latitudes, *J. Geophys. Res.*, 107(C11), 3207, DOI: 10.1029/2001JC001210
- 830 Horsburgh KL, Wilson C. (2007) Tide–surge interaction and its role in the distribution of surge residuals in the North
831 Sea, *Jour. of Geophys. Res.* 112, CO8003, DOI: 10.1029/2006JC004033
- 832 Huang NE, Shen Z, Long SR, Wu MC, Shih HH, Zheng Q, Yen NC, Tung CC, Liu HH (1998) The empirical
833 mode decomposition and the Hilbert spectrum for nonlinear and non-stationary time-series analysis *Proc. R. Soc.*
834 *Lond. A.* 454, 903-995, DOI: 10.1098/rspa.1998.0193
- 835 Huang NE, Wu Z (2008) A review on Hilbert-Huang Transform: Method and its application to geophysical studies,
836 *Rev. of GeoPhys.* 46, RG2006, 1-23, DOI: 10.1029/2007RG000228
- 837 Huber PJ Robust Statistics Hoboken, NJ: John Wiley & Sons, Inc., 1981 DOI: 10.1137/1.9781611970036.fm
- 838 Hughes TP, Baird AH, Bellwood DR, Card M, Connolly, SR, Folke C, Grosberg R, Hoegh-Guldberg O, Jackson JBC,
839 Kleypas J, Lough JM, Marshall P, Nystrom M, Palumbi SR, Pandolfi JM, Rosen B, Roughgarden J (2003)
840 Climate Change, Human Impacts, and the Resilience of Coral Reefs, *Science* 301, 929,
841 DOI: 10.1126/science.1085046
- 842 Hughes TP, Graham NAJ, Jackson JBC, Mumby PJ, Steneck RS (2010) Rising to the challenge of sustaining coral
843 reef resilience, *Trends in Ecology and Evolution*, 25, 11, DOI: 10.1016/j.tree.2010.07.011
- 844 Jay DA (2009) Evolution of tidal amplitudes in the eastern Pacific Ocean, *Geophys. Res. Lett.*, 36, L04603,
845 DOI: 10.1029/2008GL036185
- 846 Jay DA, Leffler K, Degens S, (2011) Long-term evolution of Columbia River tides, *ASCE Journal of Waterway,*
847 *Port, Coastal, and Ocean Engineering*, 137: 182-191; DOI: 10.1061/(ASCE)WW.1943- 5460.0000082
- 848 Kaup DJ (1980) A method for solving the separable initial value problem of the full three dimensional three-wave
849 interaction, *Stud. Appl. Math*, 62, 75-83
- 850 Kohl A, Stammer D, and Cornuelle B (2007) Interannual to decadal changes in the ECCO Global Synthesis. *J.*
851 *Phys.Oceanogr.*, 37, 313–337, DOI: 10.1175/JPO3014.1
- 852 Kukulka, T., and Jay DA, (2003) Impacts of Columbia River discharge on salmonid habitat II. Changes in shallow-
853 water habitat, *J. Geophys. Res.* 108, 3294 DOI: 10.1029/2003JC001829.
- 854 Lamb KG (2007) Tidally generated near-resonant internal wave triads at a shelf break, *Geophys. Res. Lett.* 34, L18607,
855 DOI: 10.1029/2007GL030825
- 856 Leffler KE, Jay DA (2009) Enhancing tidal harmonic analysis: Robust solutions, *Cont. Shelf Res.*, 29.1, 78-88, DOI:
857 10.1016/j.csr.2008.04.011

858 Legg S, J Klymak (2008) internal hydraulic jumps and overturning generated by tidal flow over a tall steep ridge, *J.*
859 *Phys. Oceanogr.*, 38, 1949-1964

860 Lelong MP, Kunze E (2013) Can barotropic tide–eddy interactions excite internal waves? *Journal of Fluid*
861 *Mechanics*, 721, 1-27, DOI: 10.1017/jfm.2013.1

862 Livezey, RE and WY Chen, (1983) Statistical field significance and its determination by Monte Carlo techniques.
863 *Mon. Wea. Review*, 111, 46-59, DOI: 10.1175/1520-0493(1983)111<0046: SFS AID>2.0.CO;2

864 Locarnini, R.A., Mishonov, A.V., Antonov, J.I., Boyer, T.P., Garcia, H.E., Baranova, O.K., Zweng, M.M. &
865 Johnson, D.R. (2010) World Ocean Atlas 2009, S. Levitus, Ed. NOAA Atlas NESDIS 67, U.S. Gov. Printing
866 Office, Wash., D.C., 184 pp

867 Lombard A, Garric G, Penduff T (2009) Regional patterns of observed sea level change: Insights from a 1/48 global
868 ocean/sea-ice hindcast, *Ocean Dyn.*, 59, 433–449, DOI: 10.1007/s10236-008-0161-6

869 MacKinnon, J. A., and K. B. Winters (2005) Subtropical catastrophe: Significant loss of low-mode tidal energy at
870 28.9N, *Geophys. Res. Lett.*, 2, L15605, DOI: 10.1029/2005GL023376

871 Merrifield MA (2011) A shift in western tropical Pacific sea level trends during the 1990s, *Jour. of Climate*, 24, 4126-
872 4138, DOI: 10.1175/2011JCLI3932.1

873 Millero FJ, F Rainer, DG Wright, TJ McDougall (2008) The composition of standard seawater and the definition of
874 the reference-composition salinity scale, *Deep Sea Res. Part 1*, 55, 1, 50-72, DOI:10.1016/j.dsr.2007.10.001

875 Mitchum GT, Chiswell SM (2000) Coherence of internal tide modulations along the Hawaiian ridge *J. Geophys.*
876 *Res.*, 105(C12), 28653–28661, DOI: 10.1029/2000JC900140

877 Müller M, Arbic BK, Mitrovica J (2011) Secular trends in ocean tides: observations and model results. *J. Geophys.*
878 *Res.*, 116, C05 013, DOI: 10.1029/2010JC006387

879 Müller M (2012) The influence of changing stratification conditions on barotropic tidal transport. *Contin. Shelf Res.*,
880 47 (15), 107-188, DOI: 10.1016/j.csr.2012.07.003

881 Nerem RS, Chambers DP, Leuliette EW, Mitchum GT, Giese BS (1999) Variations in global mean sea level associated
882 with the 1997-1998 ENSO event: Implications for measuring long term sea level change, *Geophys. Res. Lett.*
883 26(19), 3005-3008, DOI: 10.1029/1999GL002311

884 Nicholls, RJ, A Cavenaze (2010) Sea level rise and its impacts on coastal zones, *Science* 18, June 2010: 328,
885 5985 pp.1517-1520 DOI: 10.1126/science.1185782

886 Pawlowicz R, B Beardsley, S Lentz (2002) Classical tidal harmonic analysis including error estimates in MATLAB
887 using T_TIDE, *Computers and Geosciences*, 28, 8, 929-937

888 Parker, Bruce (1991) *Tidal Hydrodynamics*, John Wiley and Sons, NY, 1-883, ISBN: 978-0471514985

889 Pickering MD ,Wells NC, Horsburgh KJ, Green JAM (2010) The impact of future sea-level rise on the European
890 Shelf tides, *Cont. Sh. Res.* 35, 1-15, DOI: 10.1016/j.csr.2011.11.011

891 Pugh DT (1987) Tides, surges and mean sea-level: a handbook for engineers and scientists, Wiley, Chichester, 472pp,
892 ISBN: 978-0471915058

893 Pugh DT (2004) Changing sea levels. Effects of tides, weather and climate. Cambridge University Press, 280pp, ISBN:
894 978-0521532181

895 Ray RD, Mitchum GT (1996) Surface manifestations of internal tides generated near Hawaii. *Geophys. Res. Letters*
896 23, 2101-2104, DOI: 10.1029/96GL02050

897 Ray RD, Mitchum GT (1997) Surface manifestations of internal tides in the deep ocean: observations from altimetry
898 and island gauges, *Prog. Oceanography*, 40,135-162, DOI:10.1016/S0079-6611(97)00025-6

899 Ray RD (2001) Comparisons of global analyses and station observations of the S₂ barometric tide *Geophys. Res. Lett.*
900 28, 21-24, DOI: 10.1016/S1364-6826(01)00018-9

901 Ray RD (2006) Secular changes of the M2 tide in the Gulf of Maine, *Cont. Shelf. Res.*, 26(3), 422-427, DOI:
902 10.1016/j.csr.2005.12.005

903 Ray RD (2009) Secular changes in the solar semidiurnal tide of the western North Atlantic Ocean, *Geophysical*
904 *Research Letters*, 36, L19601, DOI: 10.1029/2009GL040217

905 Rainville L, R Pinkel (2006) Propagation of low-mode internal waves through the ocean, *J. Phys. Oceanogr.*, 36, 6,
906 1220-1236, DOI: 10.1175/JPO2882.1

907 Ropelewski CF, Halpert MS (1987) Global and regional scale precipitation patterns associated with the El Nino/
908 Southern Oscillation, *Monthly Weather Review*, 115, 1606-1626

909 Timmermann A, McGregor S, Jin FF (2010) Wind effects on past and future regional sea level trends in the southern
910 Indo-Pacific. *J. Climate*, 23, 4429–4437, DOI: 10.1175/2010JCLI3519.1

911 Weiland J Wilhelmsson H. (1977) Coherent non-linear interaction of waves in plasmas, Pergamon Press, ISBN: 978-
912 0080209647

913 White WB, Cayan DR, Dettinger MD, Auad G (2001) Sources of global warming in the upper ocean temperature
914 during El Nino, *J. Geophys. Res.*, 106(C3), DOI: 10.1029/1999JC000130

915 Wolanski, E (1994) Physical oceanographic processes of the Great Barrier Reef, CRC Press, 208pp, ISBN:
916 0849380472

917 Woodworth PL (2010) A survey of recent changes in the main components of the ocean tide, *Continental Shelf*
918 *Research*, 30(15), 1680-1691, DOI: 10.1016/j.csr.2010.07.002

919 Wu Z Huang NE (2009) Ensemble empirical mode decomposition: A noise-assisted data-analysis method, *Advances*
920 *in Adaptive Data Analysis*, 1(1), 1-41

921 Xie XH, Chen GY, Shang XD, Fang WD (2008) Evolution of the semidiurnal (M2) internal tide on the continental
922 slope of the northern South China Sea, *Geophys. Res. Lett.*, 35, L13604, DOI: 10.1029/2008GL034179

923 Zakharov VE, Manakov SV (1973) Resonant interaction of wave packets in nonlinear media, *Soviet Phys. – J.T.E.P.*
924 *Lett.* 18, 243-247

925 Zaron, E, DA Jay (2014) An analysis of secular changes in tides at open-ocean sites in the Pacific. *Accepted by Journal*
926 *of Physical Oceanography.*

927

928

929

930

931

932

933 **Table 1a** Station information for tidal records used in this study; locations are shown in Figure 1^a

Station	Country	Start Year	End Year	Environment	MSL Rates ^a	Pre-1993 ^a	Post-1993 ^a
Pohnpei	Micronesia	1974	2012	volcanic	2.22 ± 0.01	-2.20 ± 0.28	4.71 ± 0.27
Majuro	Marshall Is.	1974	2012	atoll	3.91 ± 0.15	2.66 ± 0.45	7.02 ± 0.41
Malakal	Belau	1974	2012	mountainous/reef	2.98 ± 0.15	-1.56 ± 0.44	10.36 ± 0.42
Yap	Micronesia	1974	2012	mountainous/reef	1.99 ± 0.12	-2.91 ± 0.34	7.30 ± 0.34
Honiara	Solomon Is.	1975	2012	volcanic	0.88 ± 0.08	-5.15 ± 0.24	8.51 ± 0.20
Rabaul	Pap. N. Gui.	1966	1997	volcanic	-3.16 ± 0.09	-5.94 ± 0.10	N/A
Kanton	Kiribati	1949	2012	atoll	0.89 ± 0.05	0.12 ± 0.08	4.69 ± 0.29
Noumea	France	1967	2012	reef	1.37 ± 0.09	0.53 ± 0.20	5.93 ± 0.34
Saipan	N. Mar. Is.	1978	2012	mountainous	2.27 ± 0.10	N/A	N/A
Kapinga	Micronesia	1978	2009	atoll	2.82 ± .12	N/A	N/A
Lautoka	Fiji	1992	2012	volcanic	5.58 ± 0.10	N/A	N/A
Midway	USA	1947	2012	atoll	0.86 ± 0.02	-0.25 ± 0.04	5.40 ± 0.17
Wake	USA	1950	2012	atoll	1.99 ± 0.05	1.42 ± 0.07	1.12 ± 0.36
Johnston	USA	1947	2012	atoll	0.85 ± 0.05	0.51 ± 0.06	3.04 ± 0.59
Guam	USA	1948	2012	mountainous	1.32 ± 0.04	-0.89 ± 0.06	9.32 ± 0.31
Kwajalein	Marshall Is.	1946	2012	atoll	1.72 ± 0.07	0.71 ± 0.10	8.07 ± 0.50
Pagopago	USA	1948	2012	volcanic	2.13 ± 0.05	1.45 ± 0.08	6.44 ± 0.37
Brisbane	Australia	1984	2012	estuary	2.75 ± 0.10	N/A	N/A
Bundaberg	Australia	1984	2012	estuary	1.90 ± 0.08	N/A	N/A
Ft. Denison	Australia	1914	2012	estuary/ria	0.92 ± 0.12	1.06 ± 0.22	2.84 ± 0.56
Townsville	Australia	1985	2012	coastal bay	0.81 ± 0.16	N/A	N/A
Legaspi	Philippines	1984	2007	coastal bay	8.97 ± 0.42	N/A	N/A
Cairns	Australia	1985	2010	coastal inlet	2.14 ± 0.33	N/A	N/A
Gladstone	Australia	1978	2010	coastal bay	2.47 ± 0.58	N/A	N/A
Williamstown	Australia	1966	2010	coastal bay	1.39 ± 0.07	0.09 ± 0.17	2.48 ± 0.25
Auckland	New Zealand	1904	2010	coastal bay	1.48 ± 0.09	1.33 ± 0.07	3.75 ± 0.18

934 ^a-Expressed in mm yr⁻¹. N/A indicates there was not a full nodal cycle (~18.6 years) of data before 1993 available.

935

936

937 **Table 1b** Long-term (linear) trends, with 95% confidence limits, for tidal amplitudes and phases^a

Tidal Comp:	K ₁		O ₁		M ₂		S ₂	
	A-LTT	P-LTT	A-LTT	P-LTT	A-LTT	P-LTT	A-LTT	P-LTT
Station	(mmcy ⁻¹)	(degcy ⁻¹)	(mmcy ⁻¹)	(degcy ⁻¹)	(mmcy ⁻¹)	(degcy ⁻¹)	(mmcy ⁻¹)	(degcy ⁻¹)
Pohnpei	-7.5 ± 2.5	-7.5 ± 1.7	4.4 ± 1.3	5.7 ± 1.1	22.0 ± 6.7	8.0 ± 1.8	18.2 ± 4.4	1.8 ± 2.0
Majuro	0.4 ± 2.6	17.7 ± 2.7	3.7 ± 1.5	23.2 ± 2.4	44.9 ± 8.3	0.8 ± 1.2	35.8 ± 3.8	4.6 ± 0.9
Malakal	15.7 ± 4.8	2.6 ± 1.3	-1.0 ± 3.0	-5.5 ± 2.8	62.3 ± 5.8	0.1 ± 1.2	29.5 ± 2.3	-0.7 ± 1.4
Yap	14.0 ± 3.2	4.1 ± 1.3	21.8 ± 4.6	16.3 ± 4.7	41.3 ± 6.1	10.5 ± 1.8	16.2 ± 3.1	10.6 ± 2.2
Honiara	-2.1 ± 4.9	15.6 ± 1.9	-4.8 ± 4.5	22.5 ± 9.8	-6.2 ± 5.4	17.8 ± 2.8	4.0 ± 2.7	6.8 ± 1.7
Rabaul	23.6 ± 3.9	1.0 ± 1.3	5.4 ± 3.1	0.0 ± 1.4	-13.1 ± 13.1	-0.8 ± 12.8	14.4 ± 5.6	0.8 ± 2.5
Kanton	3.0 ± 1.0	-2.4 ± 2.6	4.0 ± 0.9	6.4 ± 2.4	27.8 ± 4.8	-5.0 ± 0.8	15.3 ± 1.3	-1.5 ± 0.6
Noumea	6.9 ± 1.2	0.6 ± 0.5	0.3 ± 0.9	0.9 ± 1.2	25.3 ± 6.1	-2.5 ± 0.7	19.3 ± 2.5	-4.6 ± 0.8
Saipan	-11.2 ± 4.9	0.7 ± 1.7	1.3 ± 2.3	-0.2 ± 2.0	33.2 ± 6.7	7.6 ± 2.6	-15.8 ± 3.9	-13.4 ± 5.2
Kapinga	19.8 ± 6.3	1.7 ± 3.1	-1.5 ± 12.5	7.2 ± 5.9	49.7 ± 9.7	7.9 ± 5.7	35.1 ± 6.6	10.3 ± 5.7
Lautoka	1.8 ± 2.2	-3.5 ± 15.1	2.8 ± 2.3	-8.1 ± 8.4	36.7 ± 7.1	-5.2 ± 0.9	12.4 ± 6.0	14.1 ± 5.2
Midway	1.5 ± 0.7	0.2 ± 0.4	1.6 ± 0.5	-2.3 ± 0.5	7.4 ± 1.2	-5.5 ± 0.7	-0.3 ± 0.5	-17.2 ± 1.7
Wake	-3.4 ± 0.6	-0.7 ± 0.6	0.9 ± 0.6	2.0 ± 0.7	-11.9 ± 2.7	2.4 ± 0.5	5.7 ± 1.1	2.1 ± 0.5
Johnston	-3.9 ± 0.8	-7.0 ± 0.5	-2.0 ± 0.4	1.8 ± 0.6	2.6 ± 1.7	-4.1 ± 0.7	8.1 ± 1.4	-11.3 ± 0.7
Guam	4.7 ± 1.9	4.3 ± 0.9	-3.4 ± 1.6	3.5 ± 0.7	-0.5 ± 2.4	1.6 ± 0.6	0.1 ± 0.9	7.7 ± 1.2
Kwajalein	1.6 ± 0.6	0.4 ± 0.5	-1.0 ± 0.5	0.2 ± 0.4	-7.3 ± 1.7	0.4 ± 0.2	-0.1 ± 1.4	-1.8 ± 0.2
Pagopago	2.2 ± 0.9	0.3 ± 0.7	2.2 ± 0.9	3.8 ± 0.9	10.1 ± 2.5	-0.2 ± 0.5	1.0 ± 0.8	-1.8 ± 0.2
Brisbane	-12.9 ± 3.7	2.5 ± 1.1	-4.9 ± 3.3	6.2 ± 1.5	15.6 ± 13.6	13.9 ± 1.1	12.3 ± 7.2	9.1 ± 1.5
Bundaberg	-8.7 ± 3.1	0.3 ± 1.1	-8.3 ± 2.4	0.5 ± 1.1	2.3 ± 5.6	1.9 ± 1.2	7.9 ± 4.4	2.5 ± 1.4
Ft Denison	-1.1 ± 0.4	-0.4 ± 0.2	-0.2 ± 0.4	-0.9 ± 0.2	-27.8 ± 10.0	-2.0 ± 0.2	-5.1 ± 0.4	-3.5 ± 0.2
Townsville	3.3 ± 1.7	-1.6 ± 0.3	2.6 ± 1.2	1.1 ± 0.5	66.8 ± 3.2	-3.0 ± 0.4	9.9 ± 2.0	1.9 ± 0.4
Legaspi	-14.8 ± 6.9	0.1 ± 2.7	-28.7 ± 7.2	9.4 ± 3.8	-69.3 ± 27.6	-4.1 ± 4.1	-13.1 ± 15.1	-0.1 ± 3.4
Cairns	8.8 ± 5.7	-0.1 ± 0.8	10.2 ± 3.1	0.4 ± 0.9	49.5 ± 12.5	-1.4 ± 1.4	15.4 ± 6.0	-3.1 ± 1.7
Gladstone	-2.2 ± 3.3	0.1 ± 0.7	-8.9 ± 2.3	1.7 ± 1.1	14.1 ± 8.2	1.6 ± 0.7	57.3 ± 6.7	2.3 ± 0.8
Wllmstwn	18.2 ± 1.6	5.1 ± 1.3	7.8 ± 1.6	9.6 ± 1.7	34.8 ± 2.1	11.7 ± 1.2	6.6 ± 1.5	18.9 ± 1.8
Auckland	-1.4 ± 0.4	1.2 ± 0.3	-0.8 ± 0.3	19.5 ± 1.3	-31.7 ± 2.0	0.6 ± 0.2	-3.6 ± 0.7	1.6 ± 1.5

938 ^a Expressed as mm century⁻¹ (mmcy⁻¹) for amplitudes, or degrees century⁻¹ (degcy⁻¹) for phases. Significant values
939 are shaded grey; significant values have SNR > 2, and an absolute magnitude of >10 mmcy⁻¹ or degcy⁻¹

940

941

942

943

944 **Table 2** Amplitude tidal anomaly trends (A-TATs) with 95% confidence limits and combined A-TATs for major
 945 diurnal and semidiurnal constituents^a.

Tidal Comp: (± 95% CI)	K₁ A-TAT	O₁ A-TAT	M₂ A-TAT	S₂ A-TAT	Comb. A-TATs
Station	(mmm ⁻¹)	(mmm ⁻¹)	(mmm ⁻¹)	(mmm ⁻¹)	(mmm ⁻¹)
Pohnpei	22.9 ± 3.6	0.2 ± 2.3	-4.1 ± 12.2	-5.6 ± 3.2	13.5 ± 13.3
Majuro	7.6 ± 6.8	-17.7 ± 4.2	-21.6 ± 23.3	-0.9 ± 5.0	-32.6 ± 25.2
Malakal	46.4 ± 3.8	6.3 ± 3.4	-28.5 ± 7.2	-2.2 ± 1.5	21.9 ± 9.0
Yap	19.6 ± 4.0	3.6 ± 5.8	-39.6 ± 7.9	-9.7 ± 1.5	-26.1 ± 10.7
Honiara	-21.2 ± 6.3	-27.6 ± 4.5	65.6 ± 3.3	15.9 ± 0.8	32.7 ± 8.4
Rabaul	-24.3 ± 3.1	-8.4 ± 2.9	91.1 ± 7.5	-11.7 ± 1.8	46.7 ± 8.8
Kanton	-14.0 ± 3.6	-2.4 ± 3.7	33.0 ± 18.3	8.7 ± 2.2	25.3 ± 19.1
Noumea	23.6 ± 4.2	2.9 ± 3.3	70.9 ± 19.0	12.9 ± 3.3	110.4 ± 20.0
Saipan	-10.6 ± 8.2	8.9 ± 3.8	17.0 ± 11.1	-8.1 ± 2.6	7.2 ± 14.6
Kapinga	-18.3 ± 5.8	-20.7 ± 12.5	47.6 ± 7.7	17.4 ± 1.6	26.1 ± 15.8
Lautoka	5.4 ± 3.3	12.3 ± 2.9	21.9 ± 10.6	6.4 ± 3.8	46.0 ± 12.1
Midway	7.4 ± 3.1	-7.7 ± 2.4	6.6 ± 6.0	2.9 ± 1.1	9.1 ± 7.2
Wake	-9.0 ± 2.6	4.1 ± 2.6	-43.6 ± 11.8	-2.4 ± 2.1	-50.9 ± 12.6
Johnston	-26.1 ± 3.4	2.1 ± 2.1	-38.4 ± 8.9	-21.9 ± 2.6	-84.3 ± 10.1
Guam	-29.0 ± 4.2	-35.9 ± 2.9	-23.3 ± 5.8	1.3 ± 0.9	-86.9 ± 7.7
Kwajalein	-1.1 ± 2.6	8.2 ± 2.0	-2.7 ± 6.6	9.1 ± 2.0	13.4 ± 7.6
Pagopago	20.3 ± 3.1	2.7 ± 1.5	82.7 ± 7.7	-9.9 ± 1.1	95.8 ± 8.5
Brisbane	19.4 ± 10.2	30.3 ± 8.4	177.6 ± 28.8	15.2 ± 8.4	242.4 ± 32.8
Bundaberg	50.8 ± 10.6	1.9 ± 6.8	-32.2 ± 15.4	-9.3 ± 4.9	11.2 ± 20.5
Ft. Denison	18.1 ± 4.8	10.2 ± 4.1	-47.9 ± 11.0	-0.5 ± 1.8	-20.1 ± 12.8
Townsville	10.4 ± 11.6	1.0 ± 7.2	-4.7 ± 19.6	-6.0 ± 4.4	0.7 ± 24.3
Legaspi	-11.2 ± 7.1	-29.1 ± 6.2	-152.0 ± 21.2	26.0 ± 4.5	-166.2 ± 23.6
Cairns	15.8 ± 16.4	27.1 ± 8.0	35.5 ± 36.0	1.7 ± 6.9	80.1 ± 40.9
Gladstone	38.3 ± 10.5	6.8 ± 7.7	-34.1 ± 26.8	-23.1 ± 8.5	-12.1 ± 31.0
Wllmstown	1.0 ± 6.3	-0.1 ± 6.2	9.2 ± 8.2	9.2 ± 2.2	19.3 ± 12.3
Auckland	6.0 ± 3.0	-0.8 ± 2.3	-58.2 ± 17.2	3.4 ± 2.5	-49.5 ± 17.8

946 ^a -All values are expressed as millimeter change in tide per meter rise in MSL (mm m⁻¹). Significant values are shaded
 947 grey, based on a SNR > 2, and an absolute magnitude of > 10 mm m⁻¹

948

949

950

951

952 **Table 3** Phase anomaly trends (P-TATs) with 95% confidence limits for major diurnal and semidiurnal constituents^a.

Tidal Comp: (± 95% CI)	K ₁	O ₁	M ₂	S ₂
	P-TAT (degm ⁻¹)	P-TAT (degm ⁻¹)	P-TAT (degm ⁻¹)	P-TAT (degm ⁻¹)
Station				
Pohnpei	-18.9 ± 2.1	8.7 ± 1.6	12.1 ± 2.9	-13.9 ± 3.1
Majuro	-26.6 ± 6.4	22.0 ± 6.0	-0.3 ± 2.9	-0.2 ± 2.2
Malakal	6.7 ± 1.4	-31.3 ± 1.3	-3.7 ± 1.3	-6.5 ± 1.4
Yap	11.0 ± 1.4	57.6 ± 2.6	17.4 ± 1.8	23.0 ± 2.1
Honiara	1.8 ± 0.6	2.3 ± 7.9	28.2 ± 2.8	-16.9 ± 1.6
Rabaul	-2.0 ± 1.2	4.2 ± 1.5	-39.6 ± 10.8	3.6 ± 2.4
Kanton	-2.8 ± 10.5	32.0 ± 10.9	-7.4 ± 3.6	4.9 ± 2.6
Noumea	2.8 ± 1.9	-3.3 ± 4.3	1.0 ± 2.5	1.2 ± 3.1
Saipan	-1.6 ± 3.0	-12.9 ± 2.9	3.7 ± 4.3	-28.2 ± 9.1
Kapinga	-13.3 ± 2.8	-27.2 ± 5.4	-32.6 ± 4.5	-37.0 ± 4.0
Lautoka	23.8 ± 39.2	-10.0 ± 12.8	-2.2 ± 1.3	14.5 ± 3.4
Midway	0.8 ± 2.1	-1.1 ± 2.2	-12.3 ± 3.1	-49.8 ± 7.2
Wake	0.6 ± 2.7	10.8 ± 3.2	17.6 ± 2.1	7.8 ± 2.3
Johnston	-3.4 ± 2.9	6.0 ± 3.4	15.8 ± 3.7	-3.0 ± 3.9
Guam	18.9 ± 1.6	-4.3 ± 1.6	-1.9 ± 1.4	15.9 ± 2.8
Kwajalein	7.6 ± 1.8	-3.6 ± 1.7	-1.6 ± 0.7	-3.2 ± 0.9
Pagopago	2.9 ± 2.5	23.6 ± 3.3	17.8 ± 1.5	-6.7 ± 3.0
Brisbane	-6.9 ± 2.8	-15.1 ± 3.3	-11.9 ± 2.9	-20.7 ± 3.8
Bundaberg	-4.4 ± 4.2	0.6 ± 3.3	-3.9 ± 3.6	-6.3 ± 4.0
Ft. Denison	10.9 ± 1.9	2.2 ± 2.4	13.2 ± 2.6	17.4 ± 2.3
Townsville	6.3 ± 1.7	-0.5 ± 2.8	-0.1 ± 1.8	2.7 ± 1.7
Legaspi	3.2 ± 2.9	16.9 ± 2.7	-17.3 ± 3.5	-7.9 ± 3.2
Cairns	1.7 ± 2.3	-1.9 ± 2.6	11.9 ± 3.8	-2.3 ± 4.8
Gladstone	8.2 ± 2.2	8.7 ± 3.4	-0.9 ± 2.6	-2.1 ± 3.1
Wllmstown	-2.3 ± 5.2	-10.1 ± 6.6	-10.2 ± 5.2	-32.0 ± 6.7
Auckland	1.9 ± 2.9	22.4 ± 11.6	1.2 ± 1.4	60.3 ± 11.6

953 ^a -All values are expressed as degree change in tide per meter rise in MSL (deg/m). Significant values are shaded grey,
 954 based on a SNR >2, and an absolute magnitude of >10 degm⁻¹. Combined trends have not been calculated for phase
 955 anomaly trends, since each forcing frequency has a different period; therefore, cumulative trends may not physical
 956 meaningful

957

958

959

960

961 **Table 4** Phase variances and phase sum variances (of the IMF 4-10 combination) for Honiara and Rabaul. For
 962 Honiara, we calculate the variances for the entire time record as well as splitting the record about the year 1993^a.

<u>Honiara</u>	K₁ phase	O₁ phase	M₂ phase	Sum of	Φ(τ)
	variance	variance	variance	variances	variance
(1974-2012)	0.49	0.62	0.71	1.06	0.42
(1974-1993)	0.11	0.12	0.89	0.91	0.48
(1993-2012)	0.47	0.54	0.51	0.88	0.31
<u>Rabaul</u>					
(1966-1997)	0.15	0.20	1.56	1.58	0.68

963 ^a All variances are expressed as a percentage of a full cycle, with Φ being relative to K₁. Values shaded grey in the last column
 964 indicate that the variance is less in the combined quantity than in the sum of the individual quantities.

965
 966
 967
 968
 969
 970
 971
 972
 973
 974
 975
 976
 977

978 **Table 5a** Slopes (m/κ) of the dispersion relations of M_2 , K_1 , and O_1 at for Honiara for typical values of non-
979 dimensional N

980

N/ω_{m2}	(m/κ) <i>for M_2</i>	(m/κ) <i>for K_1</i>	(m/κ) <i>for O_1</i>
10	10.0	20.2	22.1
23	27.6	45.5	49.8
32	32.1	64.0	70.1
71	71.8	143.8	157.5
100	101.4	203.6	222.9

981

982

983

984

985

986

987

988

989

990

991

992

993

994 **Table 5b** PSI triad wavenumber estimates for three assumed depths^a.

Depth, (m)	(k,m) for M_2	(k,m) for K_1	(k,m) for O_1	Δk
500	$(2.0 \times 10^{-6}m^{-1}, \sim 0)$	$(- 2.7 \times 10^{-5}m^{-1}, \pm 1)$	$(+2.5 \times 10^{-5}m^{-1}, \pm 1)$	~ 0
5000	$(0.7 \times 10^{-6}m^{-1}, \sim 0)$	$(- 2.7 \times 10^{-5}m^{-1}, \pm 1)$	$(+2.5 \times 10^{-5}m^{-1}, \pm 1)$	$1.3 \times 10^{-6}m^{-1}$
100	$(4.0 \times 10^{-6}m^{-1}, \sim 0)$	$(-2.7 \times 10^{-5}m^{-1}, \pm 1)$	$(+2.5 \times 10^{-5}m^{-1}, \pm 1)$	$2.0 \times 10^{-6}m^{-1}$

995

996 ^a- Calculations of wavenumbers for the case of a barotropic M_2 , and a first mode baroclinic K_1 , and O_1 at Honiara, Solomon
997 Islands. Three cases are shown for three depths typical of the region; the mean depth of 500m gives an exact triad (Δk). For
998 much deeper (5000m) and much shallower (100m) water, a near-resonant triad is possible Horizontal wavenumbers (k 's, and Δk)
999 are dimensional (meters) and mode numbers are non-dimensional.

1000

1001

1002

1003

1004

1005

1006

1007

1008

1009

1010

1011

1012 **Table 5c** Baroclinic triad wavenumber estimates.

1013

<i>(k,m) for M₂</i>	<i>(k,m) for K₁</i>	<i>(k,m) for O₁</i>	Δk
$(\pm 1.1 \times 10^{-4} \text{m}^{-1}, \pm 2)$	$(\pm 8.4 \times 10^{-5} \text{m}^{-1}, \pm 3)$	$(\pm 2.5 \times 10^{-5} \text{m}^{-1}, \pm 1)$	$1.0 \times 10^{-6} \text{m}^{-1}$
$(\pm 1.1 \times 10^{-4} \text{m}^{-1}, \pm 2)$	$(\pm 2.7 \times 10^{-5} \text{m}^{-1}, \pm 1)$	$(\pm 7.8 \times 10^{-5} \text{m}^{-1}, \pm 3)$	$5.0 \times 10^{-6} \text{m}^{-1}$

1014

1015 ^a - As in Table 5b, this time for the 3-2-1 triad of Lamb (2007) (with a mode 2 M₂ wave), at Honiara, Solomon Islands. The first of
1016 the two estimates assumes that K₁ is mode 3 and O₁ is mode 1; the second assumes that K₁ is mode 1 and O₁ is mode 3.

1017

1018 **Figure Captions**

1019 **Figure 1** Bathymetry of the western Pacific Ocean, with tide gauge stations used in this study shown as white dots
1020 and bold text for island gauges, and yellow dots and italicized text for coastal gauges; the depth scale is shown at right,
1021 in meters

1022 **Figure 2** Time series of yearly average MSL (in meters) at Guam, Pago Pago, Kwajalein, Malakal, Yap, Honiara, and
1023 Kanton, showing differences in sea level evolution before and after 1993 (indicated by the dashed vertical line)

1024 **Figure 3** Amplitude anomaly trends (A-TATs) for Honiara in the Solomon Islands: (a) K_1 ; (b) O_1 ; (c) M ; (d) S_2 ; and
1025 phase anomaly trend (P-TATs) for (e) K_1 ; (f) O_1 ; (g) M_2 ; and (h) S_2 . The red bars show 95% confidence limits on
1026 each annual estimate. The green line is the robust linear regression trend, in mmm^{-1} or degm^{-1} , as shown as text, with
1027 95% confidence limits on the anomaly trend. Significance is indicated by correlation (r_0^2) values within each subplot

1028 **Figure 4** K_1 A-TAT map, showing changes in amplitude (per m MSL rise). Map backgrounds show mean tidal
1029 amplitudes (meters) over the entire time record (color scale) and phases (solid lines), from the ocean tidal model of
1030 TPXO7.2, (Egbert and Erofeeva, 2002, 2010). Red and blue colored markers show positive and negative A-TATs,
1031 respectively. The magnitudes are indicated by color intensity, as shown by legend at the bottom, in units of mm of
1032 tidal change per meter of sea level rise (mmm^{-1}). To avoid potentially spurious results due to large percentage
1033 changes in small constituents, A-TATs are only plotted if the ratio of the 95% confidence limit of the trends has an
1034 SNR > 2. Statistically insignificant values are indicated by white circles

1035 **Figure 5** O_1 A-TAT map, showing changes in amplitude anomaly trends (for a 1 meter MSL rise); symbols are as in
1036 Figure 4, and units are mmm^{-1}

1037 **Figure 6** M_2 A-TAT map, showing changes in amplitude anomaly trends (for a 1 meter MSL rise); symbols are as in
1038 Figure 4, and units are mmm^{-1}

1039 **Figure 7** S_2 A-TAT map, showing changes in amplitude anomaly trends (for a 1 meter MSL rise); symbols are as in
1040 Figure 4, and units are mmm^{-1}

1041 **Figure 8** Combined A-TAT map, showing changes in amplitude anomaly trends (for a 1 meter MSL rise); symbols
1042 are as in Figure 4, and units are mmm^{-1} . Tidal magnitudes were added together as complex quantities, and the real
1043 part of the result is what is plotted

1044 **Figure 9** Overtide ratios (ORs) for: (a) M_4/M_2^2 ; (b) M_6/M_2^3 ; (c) S_4/S_2^2 ; and (d) $MK_3/(K_1 \times M_2)$; the background color
1045 scale represents the mean OR on a logarithmic scale. For stations that show a significant change over time in this
1046 ratio, numbers and colored markers indicate change in the ORs, in units of $1/\text{m}$, (or $1/\text{m}^2$ for M_6) expressed as
1047 percentage change per year

1048 **Figure 10** Time-series for Honiara (blue line with red error bars) and Rabaul (black line with cyan error bars) of: (a)
1049 M_4 and (b) M_6 overtide ratios; and detrended (c) M_2 amplitude; (d) K_1 amplitude; and (e) O_1 amplitude; and (f) MSL
1050 at Honiara (blue) and Rabaul (black); and (g) the Multivariate El Nino Index (MEI). Horizontal lines in (f) indicate
1051 approximate threshold values of MSL at the two gauges, vertical lines indicate times of ENSO events (yellow shading),
1052 when MSL is forced below this threshold. To standardize to a common water level datum, MSL is expressed as
1053 difference from the Revised Local Reference (RLR) datum (for 1983), as defined by the Permanent Service for Mean
1054 Sea Level (PSMSL), <http://www.psmsl.org/>; MSL is 6.232m on RLR at Honiara and 6.401m at Rabaul

1055 **Figure 11** (a) Map of Solomon Islands region, with locations of tide gauges and TAO buoys used for thermocline
1056 analyses; (b) time series of D_{20} at buoys 1-3 in blue, red and green, each about equidistant to Honiara, and the
1057 composite average of all three (black dotted line); (c) time series of composite D_{20} (blue), M_2 (green) and S_2 (red)
1058 amplitude variations at Honiara; (d) time series of D_{20} (blue) at buoy 4, M_2 (green) and S_2 (red) amplitude variations
1059 at Kapingamarangi; and (e) D_{20} for Pago Pago (blue) and M_2 amplitude (green) at buoy 5. All datasets represent an
1060 IMF decomposition of monthly time series, using IMFs #4-9 out of 10 so that the long term trends are not apparent

1061 **Figure 12** K_1 TAT map, showing differences in A-TATs and P-TATs between years before 1993 and after 1993 (for
1062 a 1m MSL rise); symbols are as in Figure 4-7; values are tabulated in Table 4

1063 **Figure 13** M_2 TAT map, showing differences in A-TATs and P-TATs between years before 1993 and after 1993 (for
1064 a 1-meter MSL rise); symbols are as in Figure 4-7; values are tabulated in Table 5

1065 **Figure 14** Resonant triad interactions for Honiara (a) and Rabaul (b) in the Solomon Sea region, represented in terms
1066 of the IMF decomposition (IMFs #4-10) of the LHS (blue, $|M_2|$) and RHS (red, $\beta|O_1||K_1|$) of (13). As in Figure 9,
1067 stronger ENSO-related fluctuations are highlighted in yellow

1068 **Figure 15** Triad interactions for Honiara (a) and Rabaul (b), Solomon Sea region: scatterplots of the IMF
1069 decomposition (IMFs #4-10) of $|M_2|$ vs. $|O_1||K_1|$ to determine β in Eq. (13); 95% confidence limits and correlation (ρ)
1070 values are given

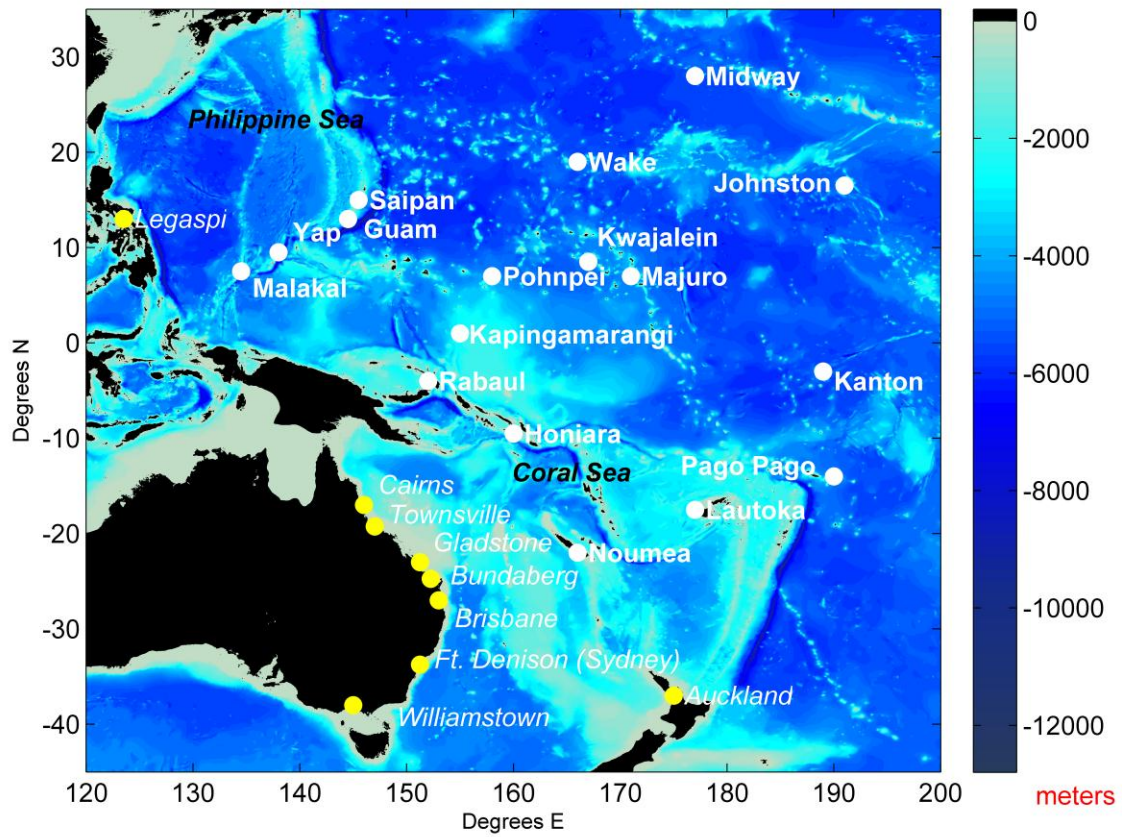
1071 **Figure 16** Phase-lock condition at Honiara, as in (2b), showing the IMF decomposition (IMFs #4-10) of the individual
1072 PD variations of M_2 (blue), K_1 (red), and O_1 (green), along with errors. The sum of the phase differences, Φ , is shown
1073 in black

1074

1075

1076

1077



1078

1079 **Figure 1** Bathymetry of the western Pacific Ocean, with tide gauge stations used in this study shown as white dots
 1080 and bold text for island gauges, and yellow dots and italicized text for coastal gauges; the depth scale is shown at right,
 1081 in meters

1082

1083

1084

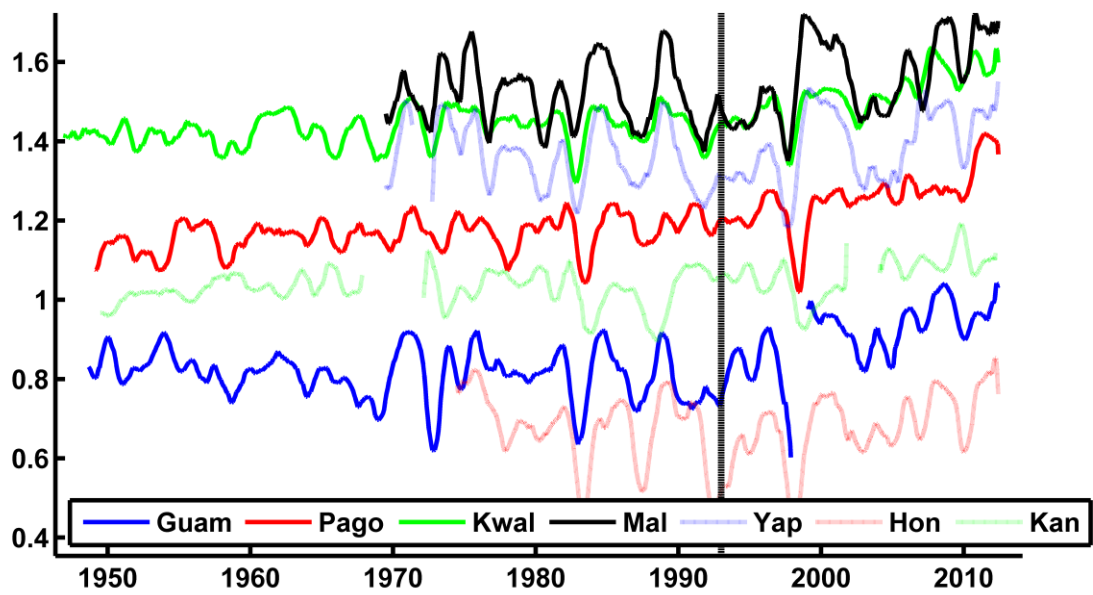
1085

1086

1087

1088

1089



1090

1091 **Figure 2** Time series of yearly average MSL (in meters) at Guam, Pago Pago, Kwajalein, Malakal, Yap, Honiara, and
 1092 Kanton, showing differences in sea level evolution before and after 1993 (indicated by the dashed vertical line)

1093

1094

1095

1096

1097

1098

1099

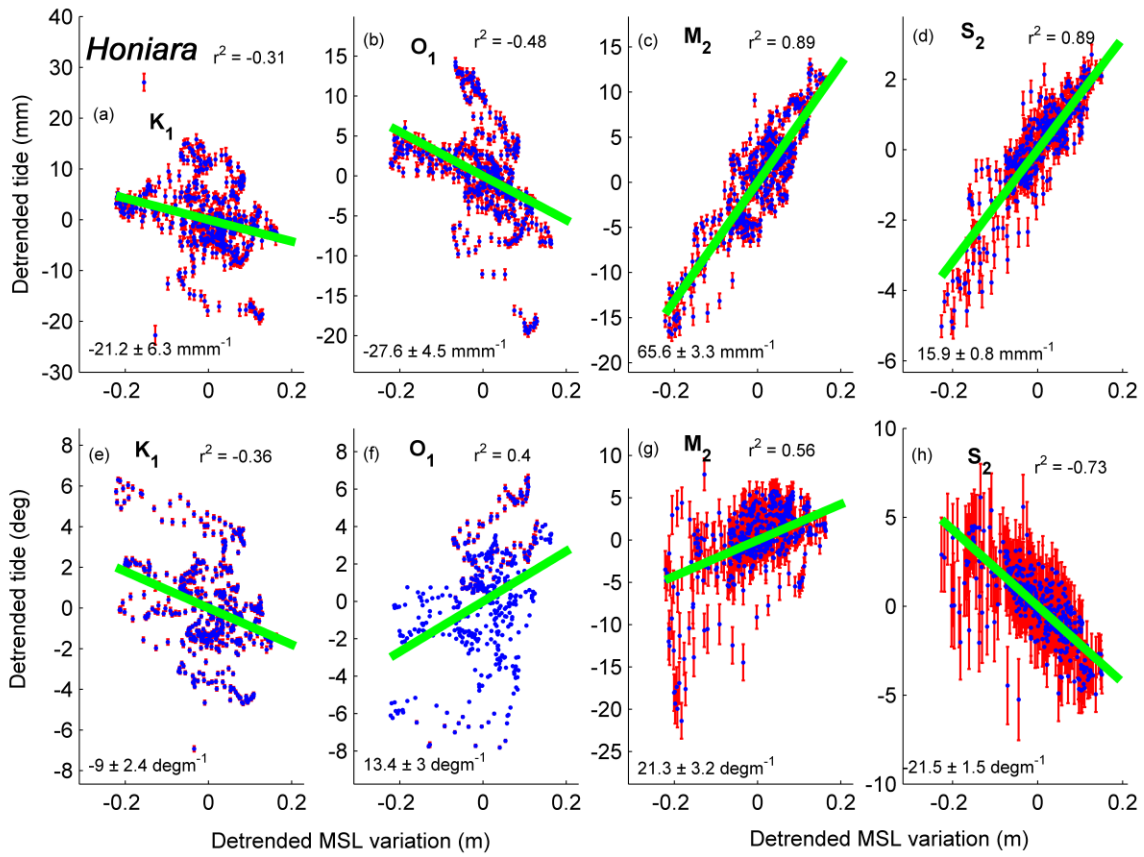
1100

1101

1102

1103

1104



1105

1106 **Figure 3** Amplitude anomaly trends (A-TATs) for Honiara in the Solomon Islands: (a) K_1 ; (b) O_1 ; (c) M_2 ; (d) S_2 ; and
 1107 phase anomaly trend (P-TATs) for (e) K_1 ; (f) O_1 ; (g) M_2 ; and (h) S_2 . The red bars show 95% confidence limits on
 1108 each annual estimate. The green line is the robust linear regression trend, in mmm^{-1} or degm^{-1} , as shown as text, with
 1109 95% confidence limits on the anomaly trend. Significance is indicated by correlation (r^2) values within each subplot

1110

1111

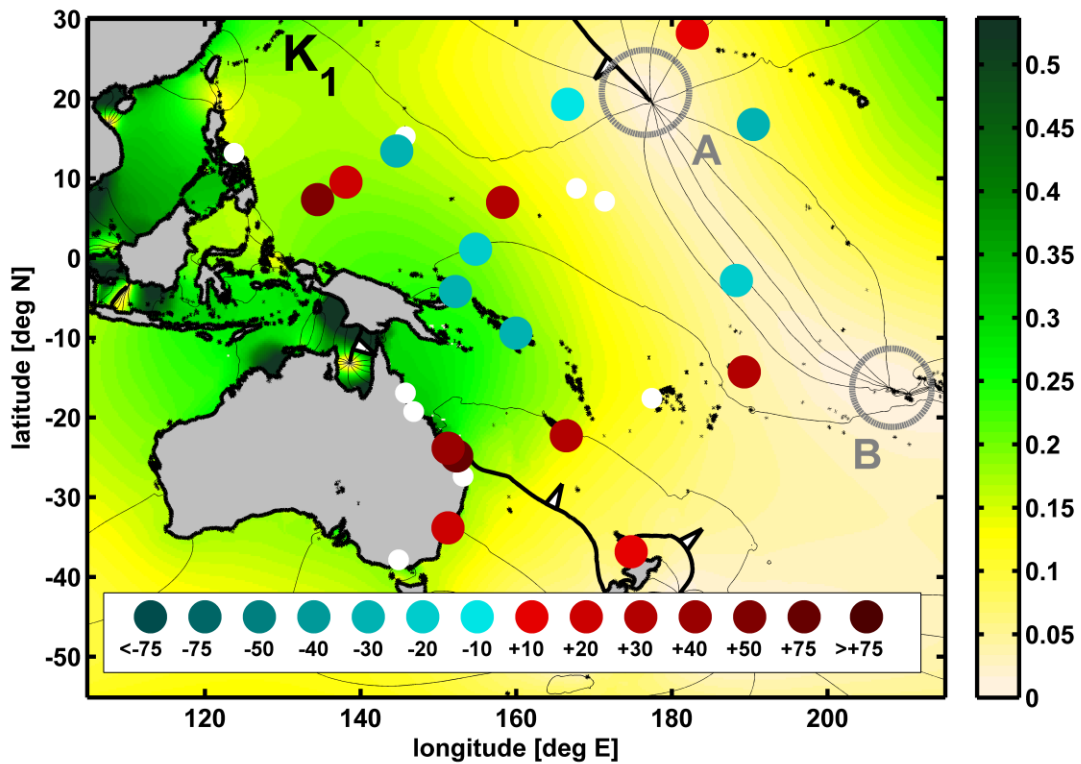
1112

1113

1114

1115

1116



1117

1118 **Figure 4** K₁ A-TAT map, showing changes in amplitude (per m MSL rise). Map backgrounds show mean tidal
 1119 amplitudes (meters) over the entire time record (color scale) and phases (solid lines), from the ocean tidal model of
 1120 TPXO7.2, (Egbert and Erofeeva, 2002, 2010). Red and blue colored markers show positive and negative A-TATs,
 1121 respectively. The magnitudes are indicated by color intensity, as shown by legend at the bottom, in units of mm of
 1122 tidal change per meter of sea level rise (mmm⁻¹). To avoid potentially spurious results due to large percentage
 1123 changes in small constituents, A-TATs are only plotted if the ratio of the 95% confidence limit of the trends has an
 1124 SNR > 2. Statistically insignificant values are indicated by white circles

1125

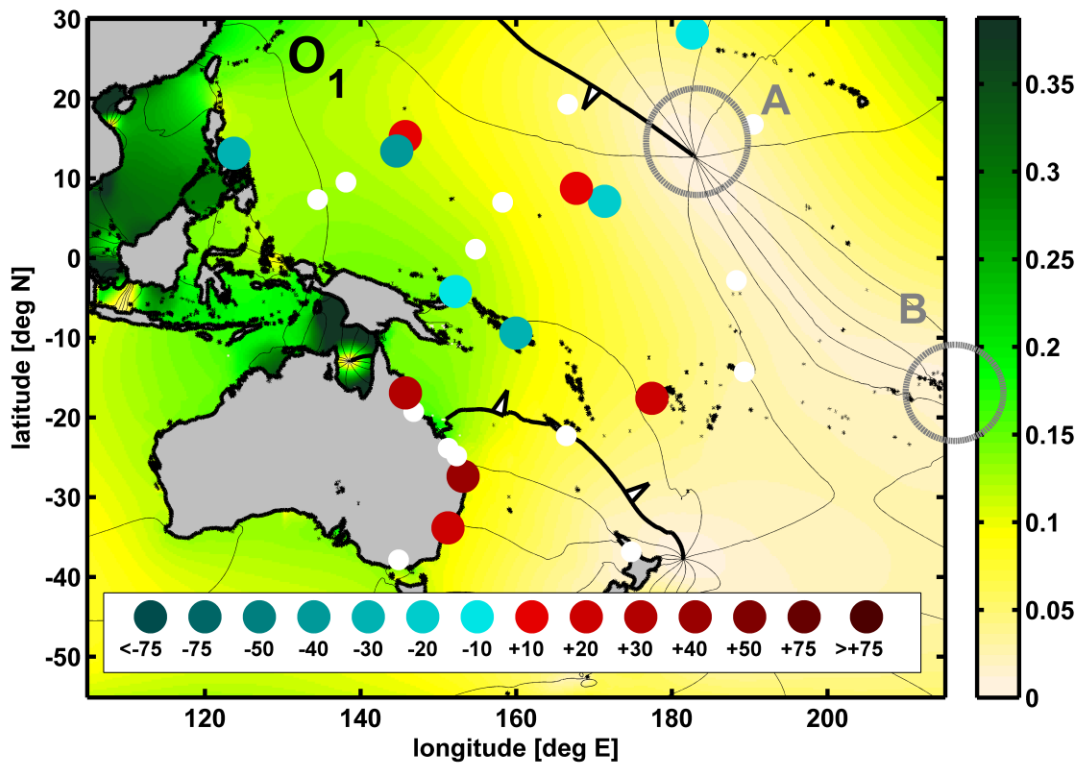
1126

1127

1128

1129

1130



1131

1132 **Figure 5** O₁ A-TAT map, showing changes in amplitude anomaly trends (for a 1 meter MSL rise); symbols are as in
 1133 Figure 4, and units are mmm^{-1}

1134

1135

1136

1137

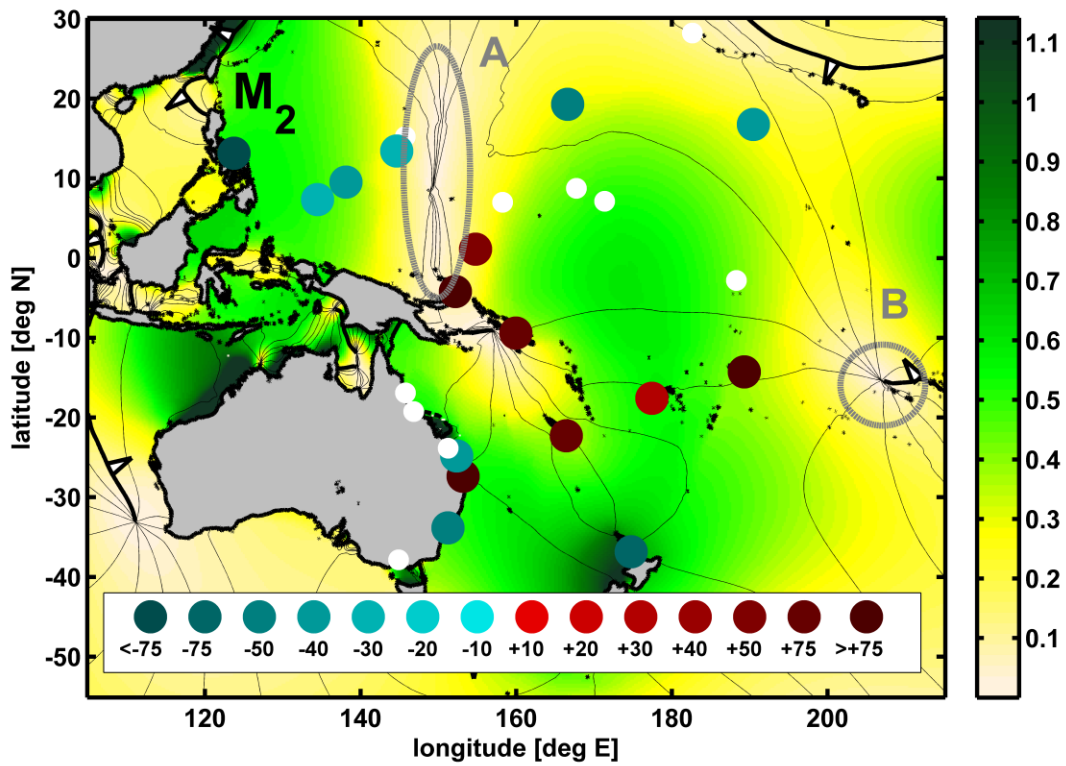
1138

1139

1140

1141

1142



1143

1144 **Figure 6** M₂ A-TAT map, showing changes in amplitude anomaly trends (for a 1 meter MSL rise); symbols are as in
 1145 Figure 4, and units are mmm⁻¹

1146

1147

1148

1149

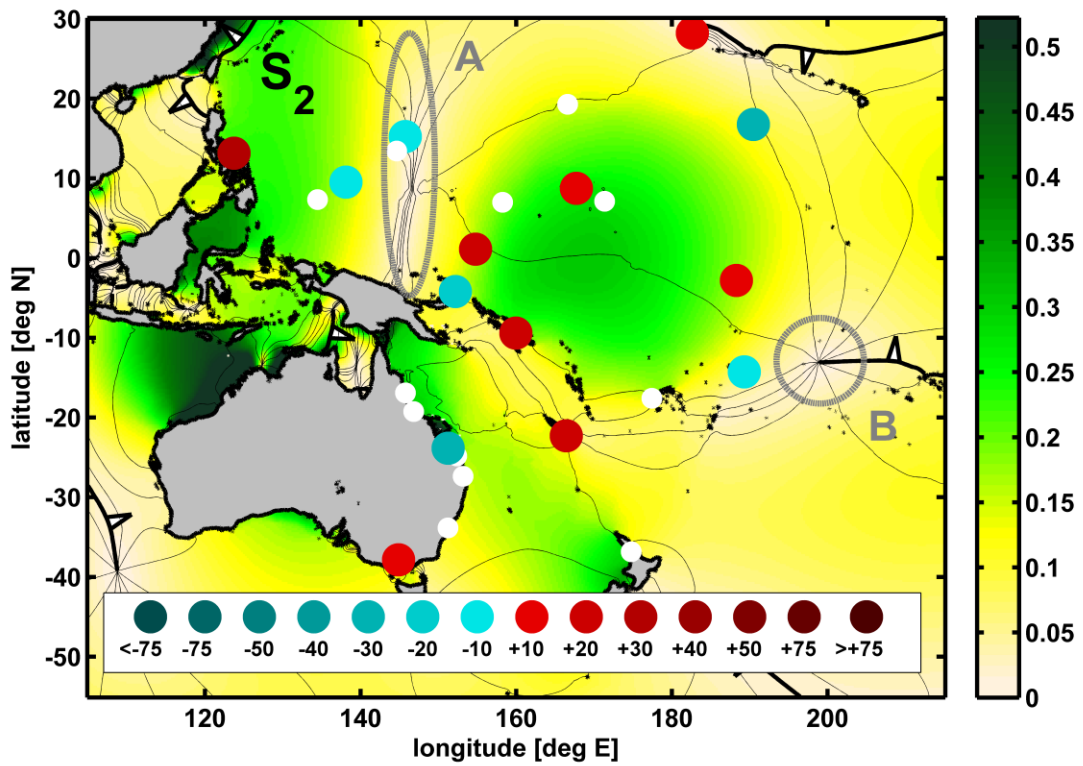
1150

1151

1152

1153

1154



1155

1156 **Figure 7** S₂ A-TAT map, showing changes in amplitude anomaly trends (for a 1 meter MSL rise); symbols are as in
 1157 Figure 4, and units are mmm^{-1}

1158

1159

1160

1161

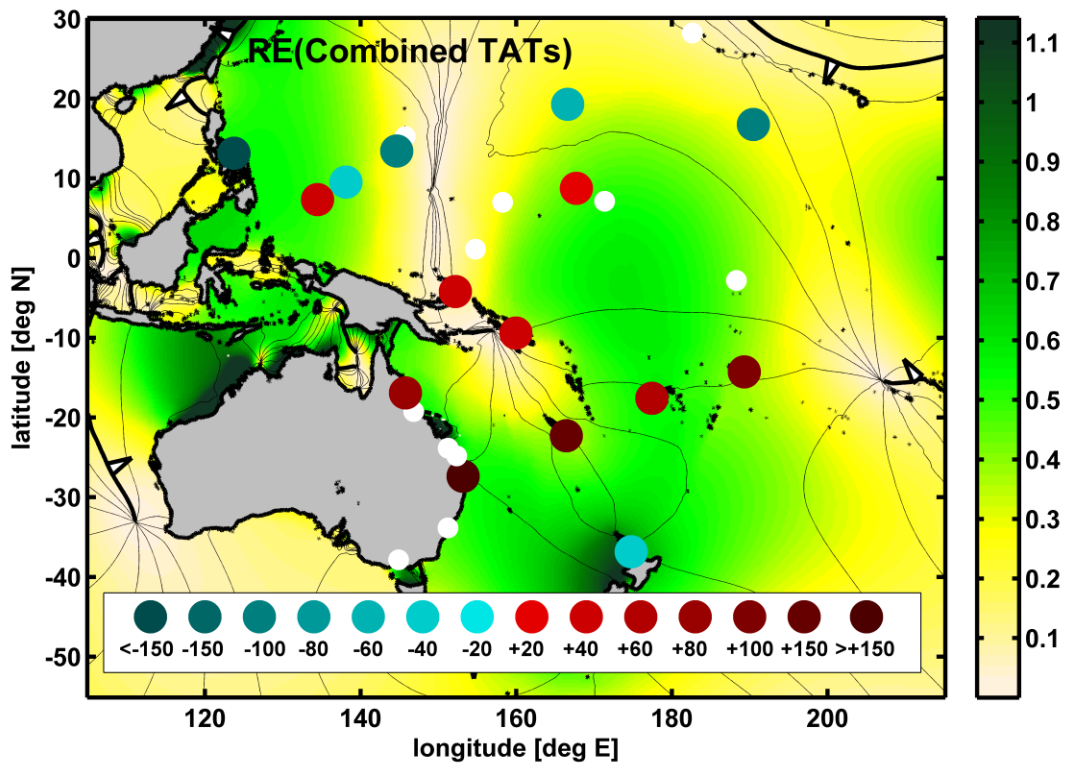
1162

1163

1164

1165

1166



1167

1168 **Figure 8** Combined A-TAT map, showing changes in amplitude anomaly trends (for a 1 meter MSL rise); symbols
 1169 are as in Figure 4, and units are mmm^{-1} . Tidal magnitudes were added together as complex quantities, and the real
 1170 part of the result is what is plotted

1171

1172

1173

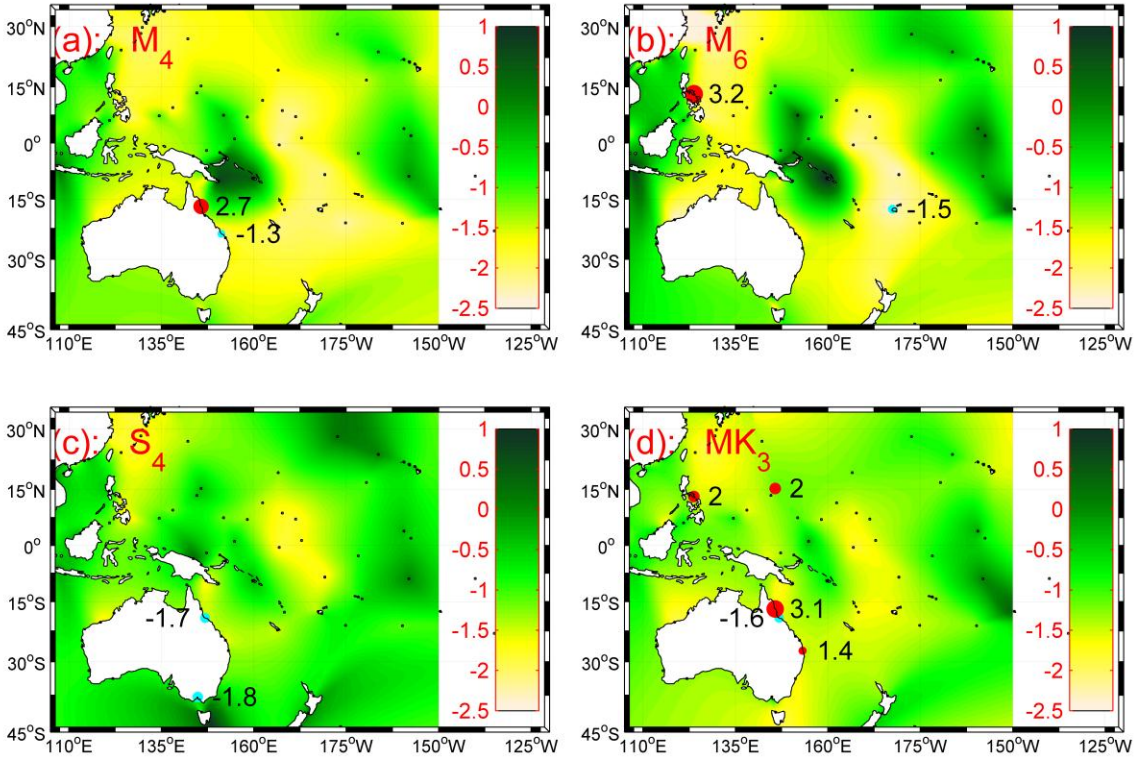
1174

1175

1176

1177

1178



1179

1180 **Figure 9** Overtide ratios (ORs) for: (a) M_4/M_2^2 ; (b) M_6/M_2^3 ; (c) S_4/S_2^2 ; and (d) $MK_3/(K_1 \times M_2)$; the background color
 1181 scale represents the mean OR on a logarithmic scale. For stations that show a significant change over time in this
 1182 ratio, numbers and colored markers indicate change in the ORs, in units of $1/m$, (or $1/m^2$ for M_6) expressed as
 1183 percentage change per year

1184

1185

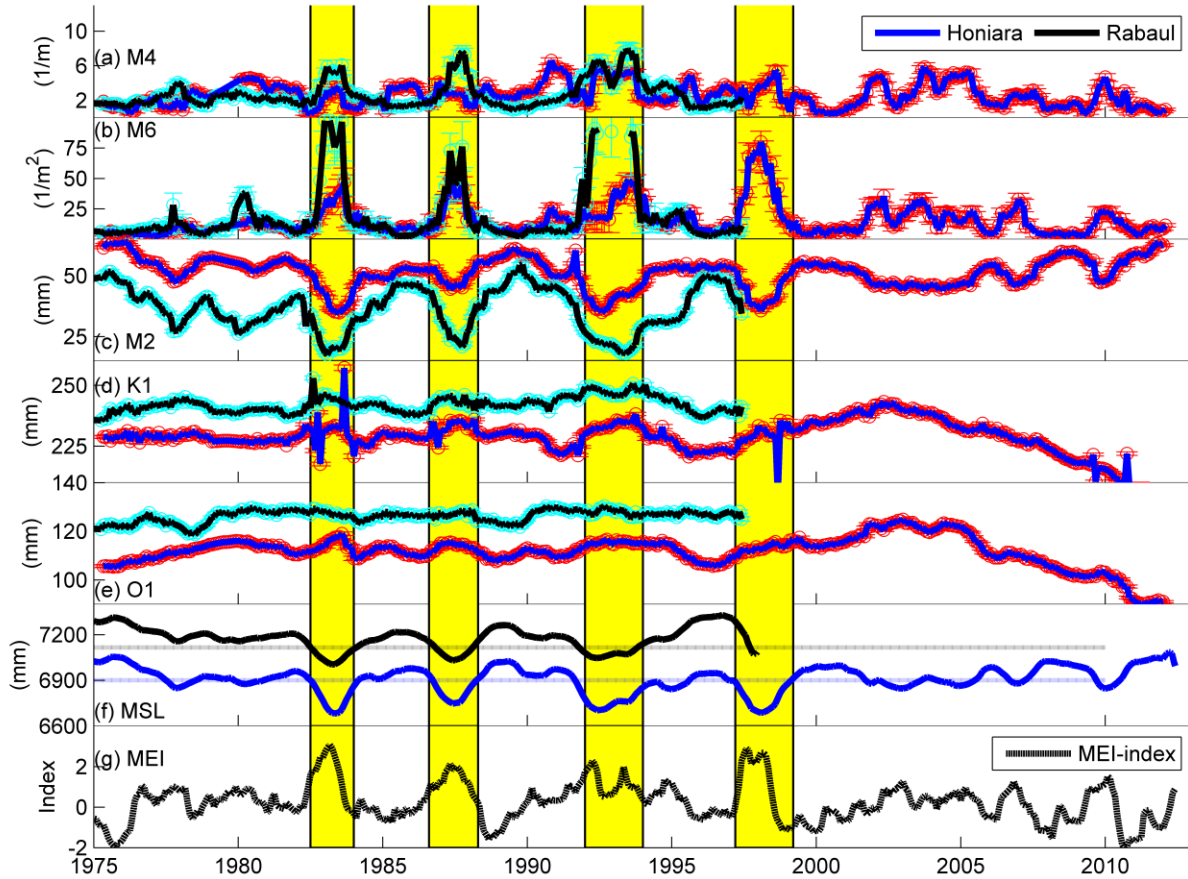
1186

1187

1188

1189

1190



1191

1192 **Figure 10** Time-series for Honiara (blue line with red error bars) and Rabaul (black line with cyan error bars) of: (a)
 1193 M_4 and (b) M_6 overtide ratios; and detrended (c) M_2 amplitude; (d) K_1 amplitude; and (e) O_1 amplitude; and (f) MSL
 1194 at Honiara (blue) and Rabaul (black); and (g) the Multivariate El Niño Index (MEI). Horizontal lines in (f) indicate
 1195 approximate threshold values of MSL at the two gauges, vertical lines indicate times of ENSO events (yellow shading),
 1196 when MSL is forced below this threshold. To standardize to a common water level datum, MSL is expressed as
 1197 difference from the Revised Local Reference (RLR) datum (for 1983), as defined by the Permanent Service for Mean
 1198 Sea Level (PSMSL), <http://www.psmsl.org/>; MSL is 6.232m on RLR at Honiara and 6.401m at Rabaul

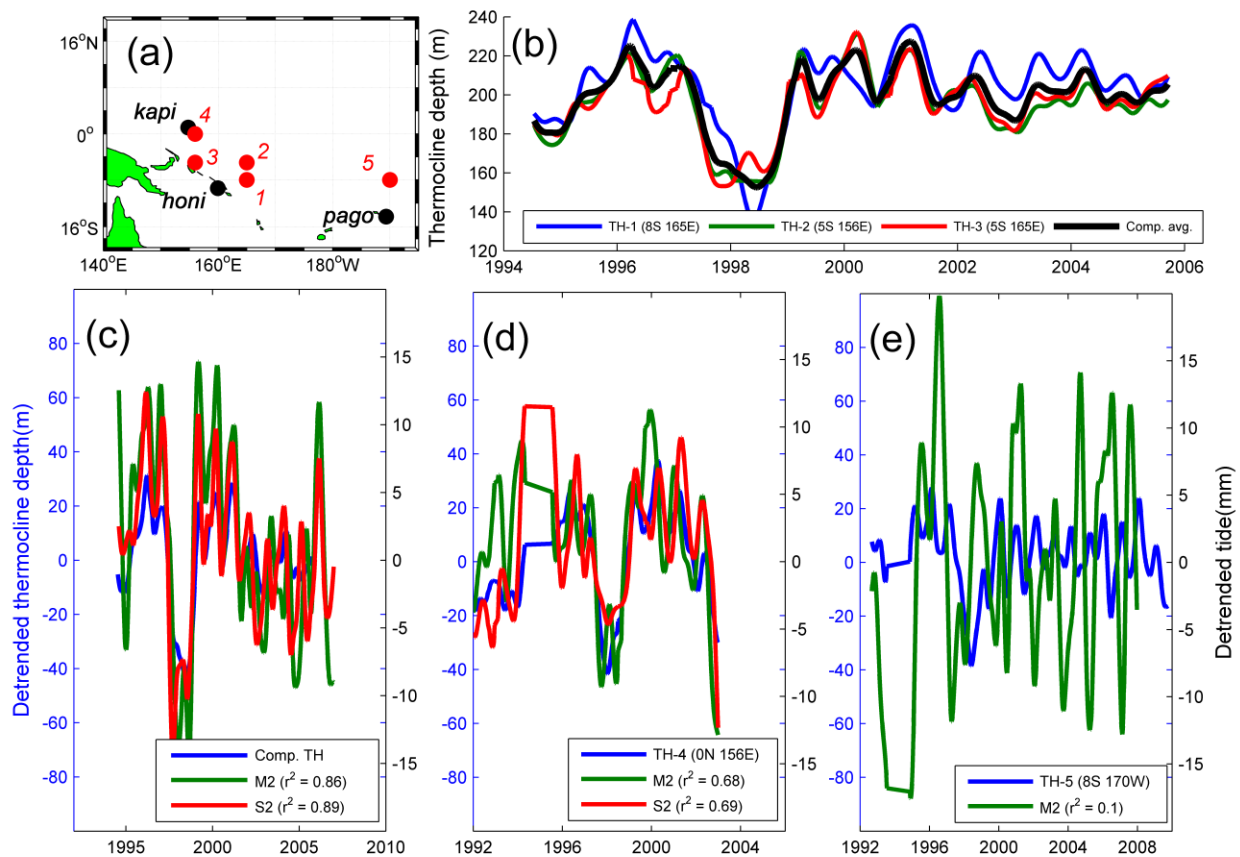
1199

1200

1201

1202

1203



1204

1205 **Figure 11** (a) Map of Solomon Islands region, with locations of tide gauges and TAO buoys used for thermocline
 1206 analyses; (b) time series of D_{20} at buoys 1-3 in blue, red and green, each about equidistant to Honiara, and the
 1207 composite average of all three (black dotted line); (c) time series of composite D_{20} (blue), M_2 (green) and S_2 (red)
 1208 amplitude variations at Honiara; (d) time series of D_{20} (blue) at buoy 4, M_2 (green) and S_2 (red) amplitude variations
 1209 at Kapingamarangi; and (e) D_{20} for Pago Pago (blue) and M_2 amplitude (green) at buoy 5. All datasets represent an
 1210 IMF decomposition of monthly time series, using IMFs #4-9 out of 10 so that the long term trends are not apparent

1211

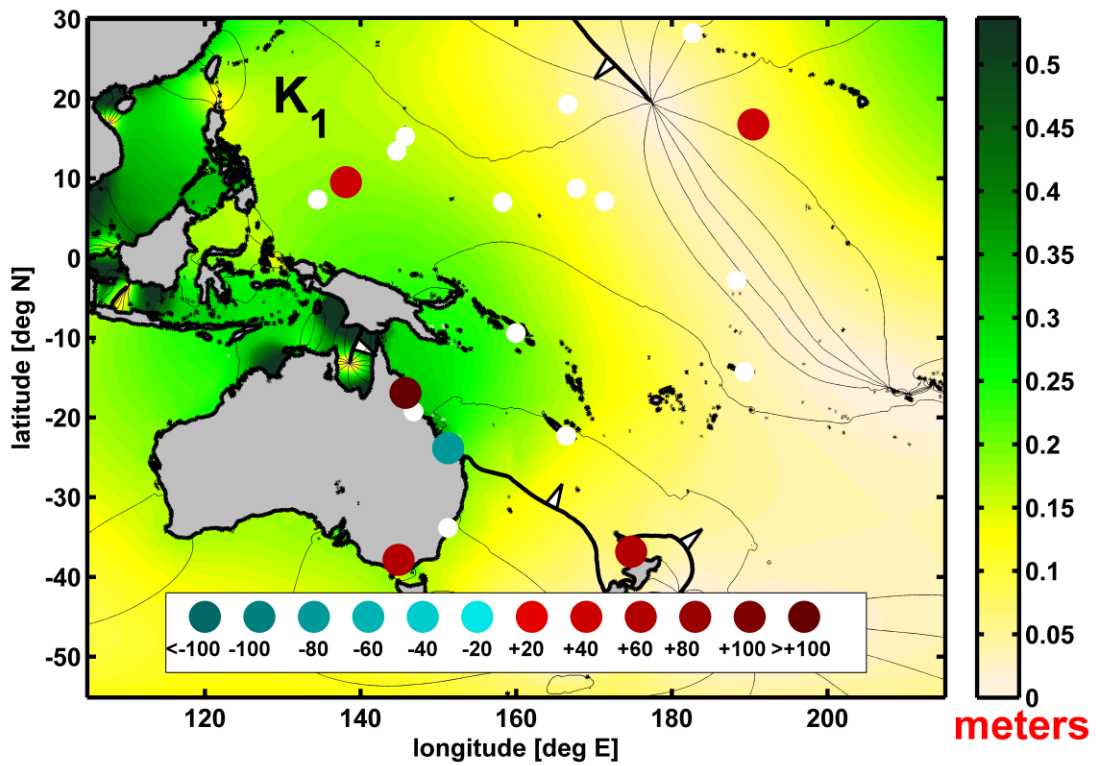
1212

1213

1214

1215

1216



1217

1218 **Figure 12** K₁ TAT map, showing differences in A-TATs and P-TATs between years before 1993 and after 1993 (for
 1219 a 1m MSL rise); symbols are as in Figure 4-7; values are tabulated in Table 4

1220

1221

1222

1223

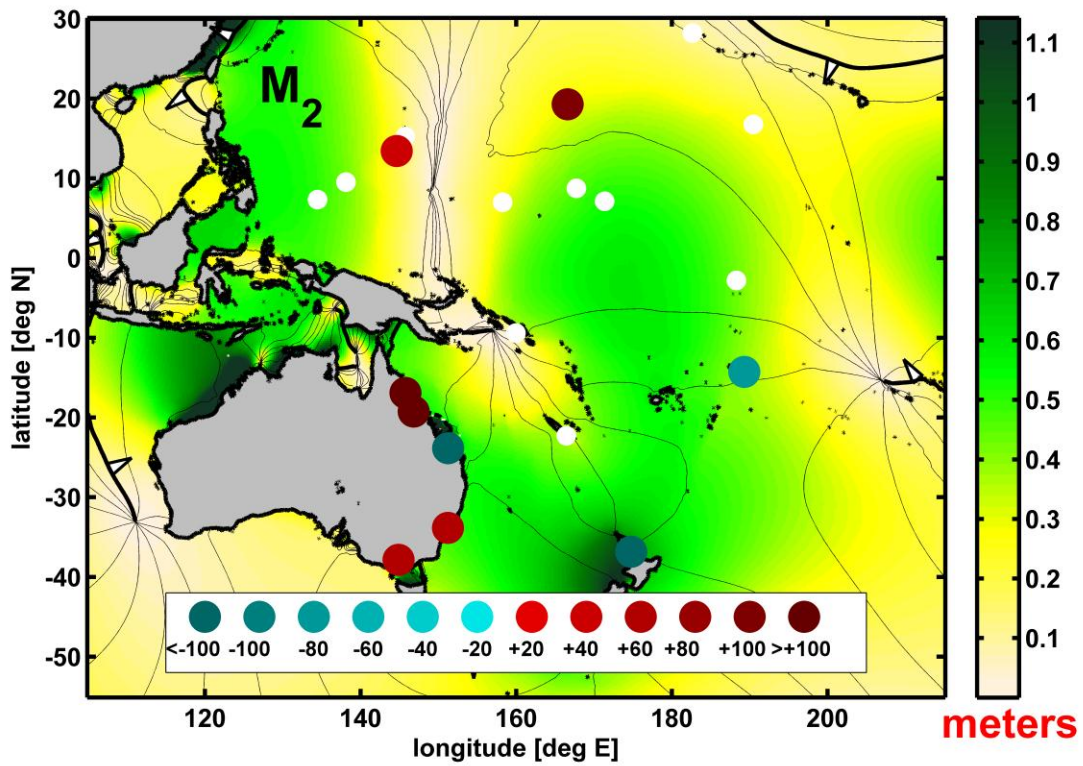
1224

1225

1226

1227

1228



1229

1230 **Figure 13** M₂ TAT map, showing differences in A-TATs and P-TATs between years before 1993 and after 1993 (for
 1231 a 1-meter MSL rise); symbols are as in Figure 4-7; values are tabulated in Table 5

1232

1233

1234

1235

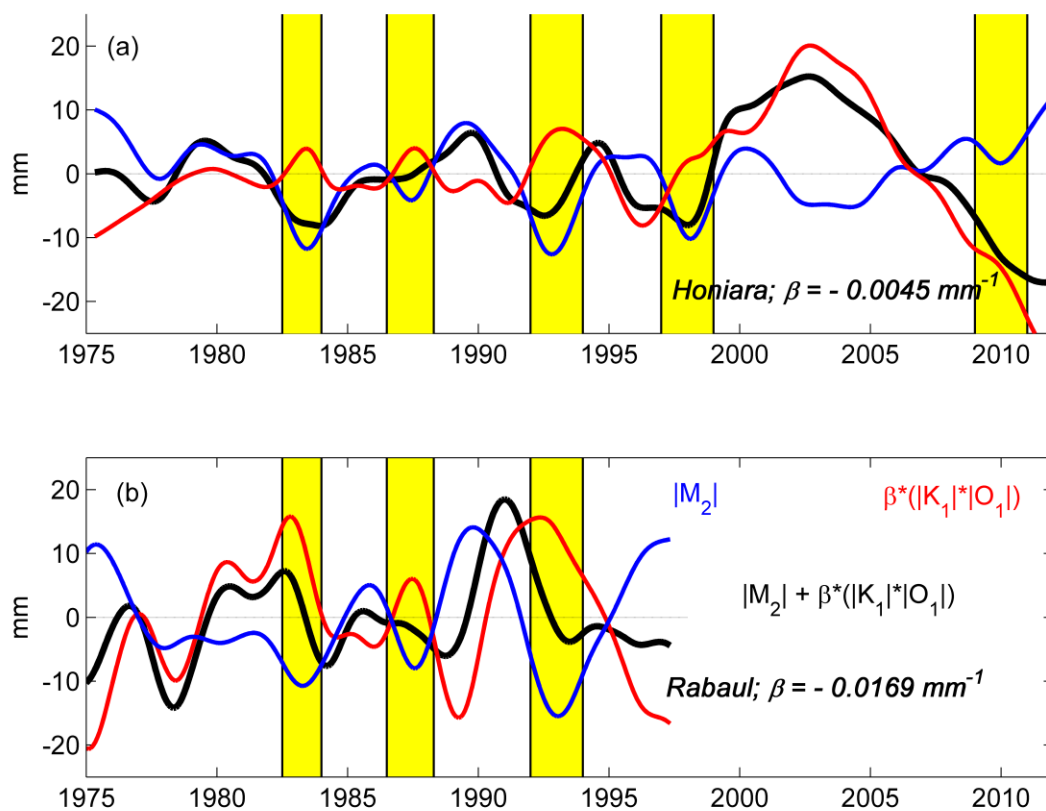
1236

1237

1238

1239

1240



1241

1242 **Figure 14** Resonant triad interactions for Honiara (a) and Rabaul (b) in the Solomon Sea region, represented in terms
 1243 of the IMF decomposition (IMFs #4-10) of the LHS (blue, $|M_2|$) and RHS (red, $\beta|O_1||K_1|$) of (13). As in Figure 9,
 1244 stronger ENSO-related fluctuations are highlighted in yellow

1245

1246

1247

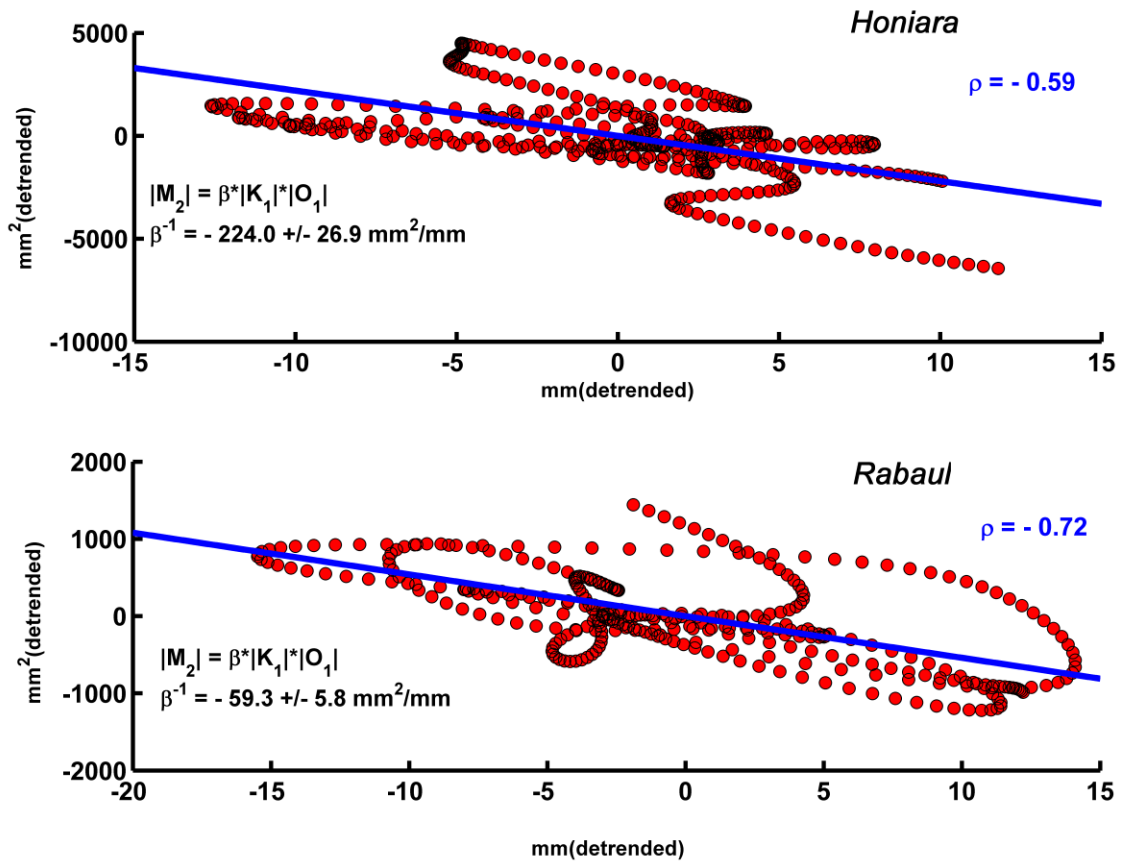
1248

1249

1250

1251

1252



1253

1254 **Figure 15** Triad interactions for Honiara (a) and Rabaul (b), Solomon Sea region: scatterplots of the IMF
 1255 decomposition (IMFs #4-10) of $|M_2|$ vs. $|O_1||K_1|$ to determine β in Eq. (13); 95% confidence limits and correlation (ρ)
 1256 values are given

1257

1258

1259

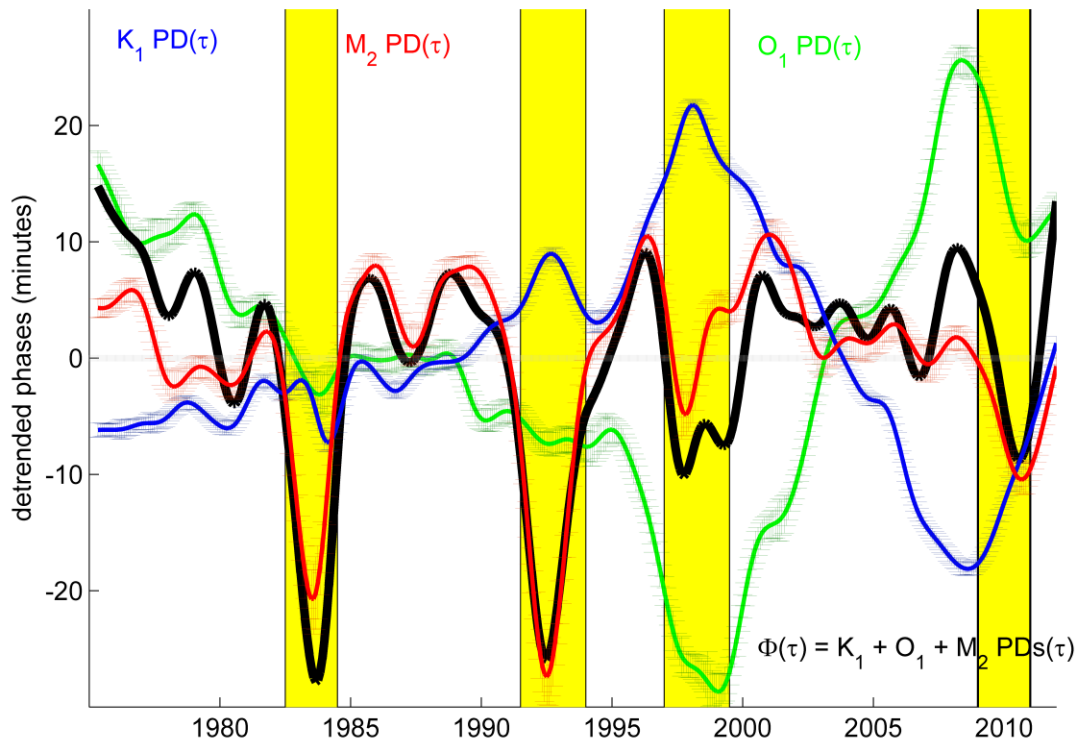
1260

1261

1262

1263

1264



1265

1266 **Figure 16** Phase-lock condition at Honiara, as in (2b), showing the IMF decomposition (IMFs #4-10) of the individual
 1267 PD variations of M_2 (blue), K_1 (red), and O_1 (green), along with errors. The sum of the phase differences, Φ , is shown
 1268 in black

1269